A weakly nonlinear mechanism for mode selection in swirling jets

Philippe Meliga, François Gallaire, Jean-Marc Chomaz

J. Fluid Mech. (2012), *vol.* 699, *pp.* 216–262.
doi:10.1017/jfm.2012.93

A weakly nonlinear mechanism for mode selection in swirling jets

Philippe Meliga[1]†, **François Gallaire**[2] **and Jean-Marc Chomaz**[3]

[1] M2P2, CNRS-Universités d'Aix-Marseille, 13451 Marseilles, France
[2] LFMI, École Polytechnique Fédérale de Lausanne, CH1015 Lausanne, Switzerland
[3] LadHyX, CNRS-École Polytechnique, 91128 Palaiseau, France

(Received 19 June 2011; revised 30 December 2011; accepted 10 February 2012;
first published online 16 April 2012)

Global linear and nonlinear bifurcation analysis is used to revisit the spiral vortex breakdown of nominally axisymmetric swirling jets. For the parameters considered herein, stability analyses single out two unstable linear modes of azimuthal wavenumber $m = -1$ and $m = -2$, bifurcating from the axisymmetric breakdown solution. These modes are interpreted in terms of spiral perturbations wrapped around and behind the axisymmetric bubble, rotating in time in the same direction as the swirling flow but winding in space in the opposite direction. Issues are addressed regarding the role of these modes with respect to the existence, mode selection and internal structure of vortex breakdown, as assessed from the three-dimensional direct numerical simulations of Ruith *et al.* (*J. Fluid Mech.*, vol. 486, 2003, pp. 331–378). The normal form describing the leading-order nonlinear interaction between modes is computed and analysed. It admits two stable solutions corresponding to pure single and double helices. At large swirl, the axisymmetric solution bifurcates to the double helix which remains the only stable solution. At low and moderate swirl, it bifurcates first to the single helix, and subsequently to the double helix through a series of subcritical bifurcations yielding hysteresis over a finite range of Reynolds numbers, the estimated bifurcation threshold being in good agreement with that observed in the direct numerical simulations. Evidence is provided that this selection is not to be ascribed to classical mean flow corrections induced by the existence of the unstable modes, but to a non-trivial competition between harmonics. Because the frequencies of the leading modes approach a strong 2:1 resonance, an alternative normal form allowing interactions between the $m = -2$ mode and the first harmonics of the $m = -1$ mode is computed and analysed. It admits two stable solutions, the double helix already identified in the non-resonant case, and a single helix differing from that observed in the non-resonant case only by the presence of a slaved, phase-locked harmonic deformation. On behalf of the finite departure from the 2:1 resonance, the amplitude of the slaved harmonic is however low, and the effect of the resonance on the bifurcation structure is merely limited to a reduction of the hysteresis range.

Key words: bifurcation, pattern formation, vortex breakdown

† Email address for correspondence: philippe.meliga@l3m.univ-mrs.fr

1. Introduction

Vortex breakdown is a widespread phenomenon occurring in swirling flows when the swirl parameter S, which compares the intensity of the azimuthal and axial velocity components, exceeds a critical value. It concerns a large variety of flows, ranging from leading-edge vortices over delta wings to atmospheric tornadoes and flame holders in combustion devices, and consists of an abrupt change in the flow topology, primarily associated with a so-called breakdown bubble with an internal stagnation point (Hall 1972; Leibovich 1978; Escudier, Bornstein & Maxworthy 1982; Escudier 1988; Billant, Chomaz & Huerre 1998). It raises a number of major concerns for the practical applications, including hysteretic behaviour and unsteadiness. As an example, the existence of multiple stable solutions has a major impact on the manoeuvrability of an aircraft, whereas the onset of unsteadiness induces structural vibrations responsible for accelerated fatigue.

In addition to the well-documented axisymmetric breakdown form involving a steady bubble enclosing a finite region of recirculating fluid, there exist spiral breakdown states characterized by well-defined helical patterns and rotational frequencies. The coexistence of axisymmetric and spiral states for the same parameter setting was first observed in the famous experiment of Lambourne & Bryer (1961) on delta wings. The distinction between states was based on flow visualizations where dye was introduced on the vortex axis: the dye filament was either found to spread symmetrically and delineate a stagnant region (axisymmetric form) or to be deformed into a spiral configuration. Since then, spiral states have also been identified by Sarpkaya (1971), Faler & Leibovich (1977) and Escudier & Zehnder (1982) in tube experiments, and by Spall & Gatski (1991) in numerical simulations of the Navier–Stokes equations.

The physical mechanisms at the origin of spiral vortex breakdown have been actively discussed to a point that some authors have even questioned the existence of spiral states and viewed them as pure visualization artifacts (see the review by Escudier 1988). Results obtained during the last decade suggest that breakdown itself does not result from the ultimate development of helical disturbances, but constitutes an independent phenomenon over which secondary helical disturbances may grow. This scenario, conjectured initially by Escudier *et al.* (1982), has been confirmed by Ruith *et al.* (2003), who performed three-dimensional (3D) direct numerical simulations (DNSs) of a Grabovski and Berger vortex (Grabowski & Berger 1976) issuing into a semi-infinite domain, and by Herrada & Fernandez-Feria (2006), who analysed similarly the dynamics of a Batchelor vortex issuing in a straight pipe. Both studies clearly stress that the early stage of breakdown is axisymmetric, and that a finite time is needed at large swirl before this flow pattern is altered by the subsequent development of large-scale spiral waves, wrapped around and behind the axisymmetric bubble. At the moderate Reynolds numbers used in these calculations, this ultimately leads to synchronized states characterized by either a single helical structure of azimuthal wavenumber $m = -1$ or a double helical structure of azimuthal wavenumber $m = -2$.

Recently, Gallaire *et al.* (2006) have used the nonlinear front theory of weakly non-parallel flows to investigate the stability properties of the axisymmetric breakdown state computed by Ruith *et al.* (2003). They have shown that the single helix observed at low swirl can be viewed as the manifestation of a so-called nonlinear 'elephant' mode, triggered by a transition from convective to absolute local instability in the lee of the axisymmetric bubble (Huerre 2000). Such an analysis yet has limitations. A first issue concerns the fact that the axisymmetric breakdown solution clearly violates the weakly non-parallel assumption. Another issue concerns the double helix observed

at larger swirl, whose existence should result from the competition between two distinct elephant modes, dictated by the interaction of their respective nonlinear fronts, a situation which lacks to date theoretical framework. The objective of the present research is therefore twofold:

(i) undertaking the global stability analysis of a Grabovski and Berger vortex and establishing a clear connection between the existence of spiral breakdown states and the linear instability of helical global modes;

(ii) performing weakly nonlinear analyses to unravel the leading mechanism responsible for selecting the helical pattern observed in the DNSs.

The outline of this paper is as follows. The flow configuration and numerical method are introduced in § 2. The spatio-temporal features of the unstable $m = -1$ and $m = -2$ global modes are presented in § 3, and the relevance of analyses based on the linear growth and nonlinear saturation of each individual mode is discussed in § 4 in view of the mode selection evidenced by Ruith *et al.* (2003). Various normal forms are computed in §§ 5 and 6 in order to discuss nonlinear mechanisms of increasing complexity. Section 5 focuses on the double-Hopf interaction, convenient to analyse classical coupling between modes in terms of mean flow corrections and harmonics generation. In § 6, we encompass an additional, non-trivial resonant interaction between the $m = -2$ mode and the first harmonic of the $m = -1$ mode, an approach motivated by the fact that both modes approach a strong 2:1 resonance. The sequences of bifurcations predicted by the normal forms are analysed and the pattern and symmetries of the stable solutions are compared with that observed in the DNSs. Physical interpretations for the observed dynamical behaviours are proposed in § 7.

2. Problem formulation

2.1. *Flow configuration*

In the following, we use standard cylindrical coordinates r, θ and z. We consider a homogeneous, incompressible fluid of kinematic viscosity ν, whose motion is described by a state vector $\boldsymbol{q} = (\boldsymbol{u}, p)^{\mathrm{T}}$, with p the pressure and $\boldsymbol{u} = (u, v, w)^{\mathrm{T}}$ the 3D velocity field of radial, azimuthal and axial components u, v and w. We investigate the dynamics of a Grabovski and Berger vortex (Grabowski & Berger 1976) whose non-dimensional azimuthal, radial and axial velocities are

$$u(r) = 0, \quad v(r) = S\Psi(r), \quad w(r) = 1, \tag{2.1}$$

using the uniform jet velocity and the jet characteristic core radius as reference scales. In (2.1), the swirl number S is the non-dimensional axial vorticity on the axis and Ψ is the piecewise function reading

$$\Psi(r \leqslant 1) = r(2 - r^2) \quad \text{and} \quad \Psi(r > 1) = 1/r. \tag{2.2}$$

We restrict here to positive swirl only, meaning that the vortex winds in space in the direct sense defined by the right-hand rule with respect to the axial direction (in other words, the flow rotates counterclockwise when viewed from the downstream z-direction). The vortex dynamics is governed by the 3D Navier–Stokes equations

$$\partial_t \boldsymbol{u} + \boldsymbol{\nabla u} \cdot \boldsymbol{u} + \boldsymbol{\nabla} p - \frac{1}{Re}\nabla^2 \boldsymbol{u} = \boldsymbol{0}, \tag{2.3a}$$

$$\boldsymbol{\nabla} \cdot \boldsymbol{u} = 0, \tag{2.3b}$$

written in compact form as

$$\mathscr{N}\,\partial_t \boldsymbol{q} + \mathscr{M}(\boldsymbol{q}) = \boldsymbol{0}, \tag{2.4}$$

with Re the Reynolds number and $\mathscr{M}$ the nonlinear evolution operator.

2.2. *Methodology*

We investigate the existence of spiral breakdown states in the framework of bifurcation theory, and retrieve the temporal and spatio-temporal instability properties from linear and weakly nonlinear stability analysis in which the flow field $\boldsymbol{q}$ is expanded into

$$\boldsymbol{q} = \boldsymbol{q}_0 + \epsilon \boldsymbol{q}_1 + \epsilon^2 \boldsymbol{q}_2 + \epsilon^3 \boldsymbol{q}_3 + \cdots \tag{2.5}$$

ϵ being the order of magnitude of the flow disturbances, assumed to be small. For the sake of readability, only the main ingredients are briefly outlined here, and exhaustive details are provided in the appendices.

Since the system possesses the symmetry group $SO(2)$, its base state $\boldsymbol{q}_0$ is a steady axisymmetric solution of the governing equation, hence satisfying

$$\mathscr{M}_0(\boldsymbol{q}_0) = \boldsymbol{0}, \tag{2.6}$$

where the subscript 0 indicates that the evolution operator is used in its axisymmetric form obtained by forcing all θ derivatives to zero.

In the linear framework, one aims at characterizing the stability of the leading-order disturbances $\boldsymbol{q}_1$, expanded in terms of normal modes according to

$$\boldsymbol{q}_1 = \hat{\boldsymbol{q}}(r,z)\mathrm{e}^{\mathrm{i}m\theta+(\sigma+\mathrm{i}\omega)t} + \hat{\boldsymbol{q}}^*(r,z)\mathrm{e}^{-\mathrm{i}m\theta+(\sigma-\mathrm{i}\omega)t}. \tag{2.7}$$

In (2.7), $\hat{\boldsymbol{q}} = (\hat{\boldsymbol{u}}, \hat{p})^{\mathrm{T}}$ is the so-called global eigenmode of growth rate σ and pulsation ω, and the superscript $*$ indicates complex conjugation. Linearization of (2.4) around the base flow yields the system of equations governing the global mode under the form of a generalized eigenvalue problem reading

$$((\sigma + \mathrm{i}\omega)\mathscr{N} + \mathscr{L}_m)\,\hat{\boldsymbol{q}} = \boldsymbol{0}, \tag{2.8}$$

with $\mathscr{L}_m$ the m-th Fourier form of the Jacobian, i.e. the linearized evolution operator $\mathscr{L} = \partial\mathscr{M}/\partial\boldsymbol{q}$ obtained by replacing all θ derivatives by products by im.

In the nonlinear framework, one aims at deriving a system of equations ruling the amplitude of the unstable global modes, the so-called normal form. Owing to the symmetries of the system, the normal form is known *a priori* as the leading-order system of polynomial differential equations remaining invariant under translation in time by t_0 ($t \to t + t_0$) and rotation by θ_0 ($\theta \to \theta + \theta_0$). The coefficients of the polynomial are however unknown and cannot be estimated easily using transient dynamics computed by DNSs (Provansal, Mathis & Boyer 1987), on behalf of the large number of degrees of freedom (up to 16 in present case). Consequently, the present normal forms are derived from thorough asymptotic expansions undertaken in the vicinity of the instability threshold, which allows all coefficients to be computed analytically from the solutions $\boldsymbol{q}_i$ coming at successive orders in ϵ. The approach will also be shown to provide additional insight into the flow physics by granting access to individual mean flow corrections and harmonics computed exactly as part of the second-order solution $\boldsymbol{q}_2$.

2.3. *Numerical method*

The computational domain shown in figure 1 consists of a pipe of finite length z_{max} and radius r_{max}. The vortex profile (2.1) is prescribed at the inlet Γ_{in}, located at $z = 0$.

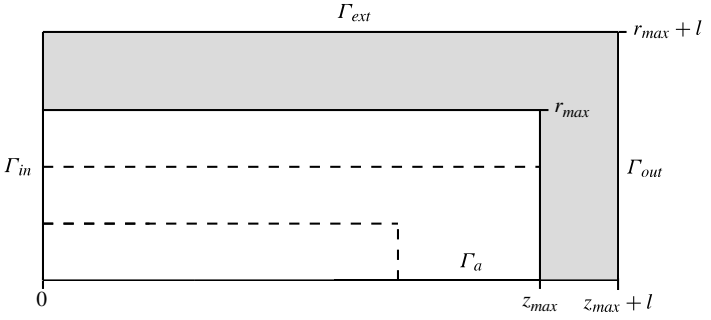

FIGURE 1. Schematic of the computational domain: the inner dashed lines delimit regions characterized by different vertex densities. r_{max} and z_{max} stand for the radius and length of the computational domain. The inlet, outlet and external boundaries are located at $z = 0$, $z = z_{max} + l$ and $r = r_{max} + l$ respectively, where l is the size of the sponge region used in the numerics, shown as the light grey shaded area.

In order to apply appropriate far-field conditions, the dimensions of the computational pipe are extended to $z_{max}+l$ and $r_{max}+l$, these values defining the position of the outlet and external boundaries denoted by Γ_{out} and Γ_{ext}, respectively. The domain in between, shown as the light grey shaded area in figure 1, is a sponge region in which the radial and azimuthal velocity components are progressively damped down to negligible levels by means of artificial dissipation. In practice, we impose a progressive grid stretching and smoothly decrease the Reynolds number to the small value $Re_s = 0.1$ at the end of the domain. The Reynolds number in all equations should therefore be replaced by a computational Reynolds number $\widetilde{Re}$ defined by

$$\widetilde{Re}(r,z) = Re \ \text{ if } r \leqslant r_{max} \text{ and } z \leqslant z_{max}, \quad (2.9a)$$

$$\widetilde{Re}(r,z) = Re + (Re_s - Re)\zeta(z, z_{max}) \ \text{ if } r \leqslant r_{max} \text{ and } z > z_{max}, \quad (2.9b)$$

$$\widetilde{Re}(r,z) = \widetilde{Re}(r_{max}, z) + (Re_s - \widetilde{Re}(r_{max}, z))\zeta(r, r_{max}) \ \text{ if } r > r_{max}, \quad (2.9c)$$

where ζ is the function defined by

$$\zeta(a,b) = \frac{1}{2} + \frac{1}{2}\tanh\left\{\tau\tan\left(-\frac{\pi}{2} + \pi\frac{|a-b|}{l}\right)\right\}, \quad (2.10)$$

along with $\tau = 4$. In return, the fluid reaches the end of the domain under the form of a uniform axial flow for which we impose a free slip condition $u = v = \partial_r w = 0$ on Γ_{ext}, and a free-outflow condition $(-p\boldsymbol{I} + Re_s^{-1}\boldsymbol{\nabla u})\cdot\boldsymbol{n} = \boldsymbol{0}$ on Γ_{out}, with $\boldsymbol{n}$ the outward-pointing vector normal to the domain. Finally, the boundary conditions at the revolution axis are derived for each specific azimuthal wavenumber from mass and momentum conservation as $r \to 0$.

All equations are solved using the finite-element solver presented in details in Meliga & Gallaire (2011) and based on the FreeFem++ software (Hecht *et al.* 2011). All matrix inversions are performed by a direct LU solver (UMFPACK package, see Davis 2004). Axisymmetric base flows are obtained by the Newton method, while eigenvalue calculations make use of Krylov methods (ARPACK package, see Lehoucq, Sorensen & Yang 1998). Although specified otherwise, all global modes are normalized by imposing the phase and the amplitude, namely $\hat{u}(0.5, 2)$ is first made real positive, and the energy is subsequently set to unity in the computational domain

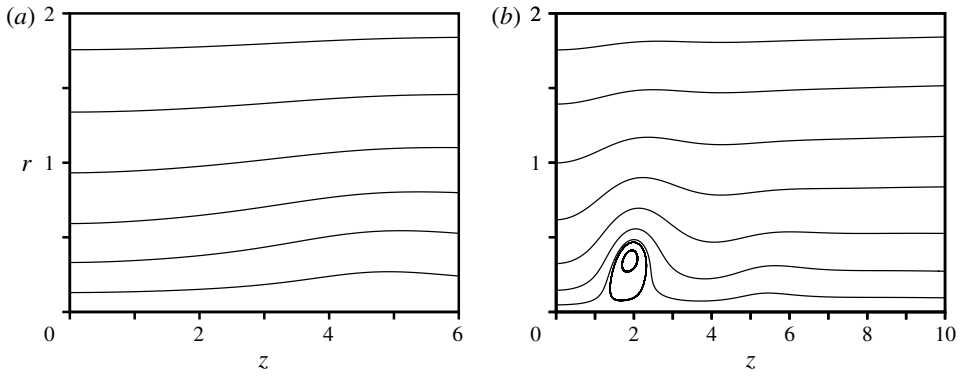

FIGURE 2. (*a*) Streamlines of the steady state prior to axisymmetric vortex breakdown, $Re = 200$, $S = 0.85$. (*b*) Same as (*a*) next to vortex breakdown, $Re = 200$, $S = 1$.

according to

$$\int_{\Sigma} |\hat{\boldsymbol{u}}|^2 \, r \, \mathrm{d}r \, \mathrm{d}z = 1. \tag{2.11}$$

In order to assess accuracy of the numerics with respect to the discretization, six meshes labelled from M_1 to M_6 differing by their spatial extent and resolution have been used. Comparative calculations documented in appendix E demonstrate especially that the results are insensitive to the use of sponge regions and thereby assess the ability of our numerics to reproduce the results obtained by Ruith *et al.* (2003), even though these authors employed advective conditions more suited to their finite differences scheme at the external and outlet boundaries. In the following, we present results obtained using the same mesh M_1 built with $r_{max} = 10$, $z_{max} = 70$ and $l = 50$, resulting in roughly 280 000 triangles whose size varies from $1/45$ close to the axis ($r \leqslant 2$) to $5/3$ at the boundary of the sponge region ($r = 60$), hence resulting in approximately 2.8 million degrees of freedom.

3. Spiral vortex breakdown as a linear instability of helical global modes

3.1. *Axisymmetric breakdown of the columnar vortex*

Our analysis focuses on a wide range of swirl $0.8 \leqslant S \leqslant 1.8$, and moderate Reynolds numbers $Re \leqslant 300$. Typical base solutions are represented in figure 2, with either smooth patterns characteristic of a columnar vortex (low swirl, see figure 2*a* at $Re = 200$, $S = 0.85$) or a well-defined bubble with front and rear stagnation points, typical of a broken down vortex (larger swirl, see figure 2*b* at $Re = 200$, $S = 1$). The development of the recirculation region can be monitored using the minimum axial velocity $w_{0,min}$ defined as

$$w_{0,min} = \min\{w_0 \mid r \leqslant r_{max}, z \leqslant z_{max}\}. \tag{3.1}$$

The diagram obtained varying the swirl and keeping the Reynolds number constant ($Re = 200$) is depicted in figure 3(*a*). The minimum velocity $w_{0,min}$ progressively decreases as the swirl increases, until it becomes zero at $S = 0.890$. This value is the threshold swirl at which the vortex breaks down, and exhibits excellent agreement with that $S = 0.8944$ reported by Ruith *et al.* (2003), the discrepancy being less than 5‰. Eigenvalue calculations restricted to steady axisymmetric modes show that the

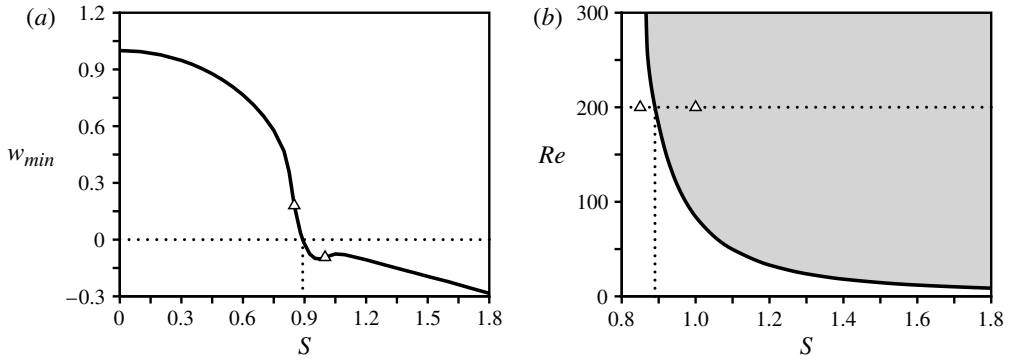

FIGURE 3. (*a*) Evolution of the minimum axial velocity $w_{0,min}$ defined by (3.1) when increasing the swirl and keeping the Reynolds number constant and equal to $Re = 200$. The value $S = 0.890$ at which the vortex breaks down is marked by the vertical dotted line. (*b*) Domain of existence of the axisymmetric breakdown solution in the (S, Re)-plane (grey shade). The horizontal and vertical dotted lines indicate respectively the Reynolds number $Re = 200$ used to produce the cut shown in (*a*), and the swirl $S = 0.890$ at which the vortex breaks down. For both plots, the symbols mark data points used to produce the axisymmetric streamlines shown in figure 2.

transition occurs without any instability, as is generally acknowledged in the literature. Such diagrams can be similarly computed for any value of the Reynolds number, which allows mapping of the domains of existence of the axisymmetric solutions in the (S, Re)-plane. The obtained results are synthesized in figure 3(*b*), with domains of existence reported for the columnar solution (white shade) and the breakdown solution (grey shade). The delimiting curve is monotonically decreasing, consistently with the idea that the large Reynolds and swirl numbers promote the occurrence of vortex breakdown.

3.2. *Spatio-temporal features of spiral modes*

Eigenvalue calculations show that all steady and time-periodic axisymmetric modes are stable for the parameters considered herein, even at the largest swirl and Reynolds numbers. In contrast, we have identified several Hopf bifurcations involving time-periodic, helical modes ($\omega \neq 0$, $m \neq 0$) shown in the following to correspond to spiral perturbations, best understood in terms of pure helical waves. The winding sense of the spiral is deduced from the sign of the product $m\varphi$ physically related to that of the axial phase velocity, $\varphi = \pm\pi/2$ denoting here the phase shift between the real and imaginary parts of the global mode. If the product is positive, disturbances wind in space clockwise when travelling in the z-direction, i.e. in the direction opposite to the swirling flow. If the product is negative, disturbances then wind in space counterclockwise, i.e. in the same direction as the swirling flow. Similarly, the rotation direction is deduced from the sign of the azimuthal phase velocity ω/m. If positive, disturbances rotate in time clockwise when travelling in the z-direction, i.e. in the direction opposite to the swirling flow. If negative, disturbances then rotate in time counterclockwise, i.e. in the same direction as the swirling flow. Expression (2.7) readily displays the real nature of the perturbation, and shows that it may be equivalently represented by either (σ, ω, m) or $(\sigma, -\omega - m)$. Since complex conjugation reverses simultaneously the signs of φ, m and ω, the winding and

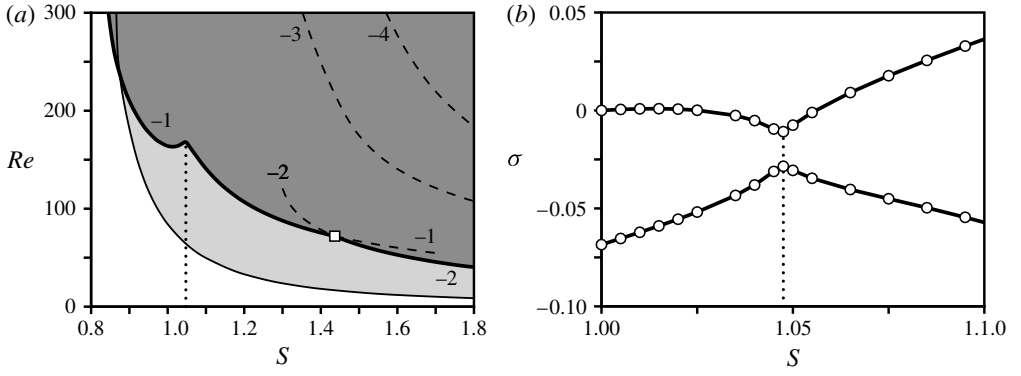

FIGURE 4. (*a*) Boundary separating the unstable domain (dark grey shade) from the stable domain in the (S, Re)-plane. The thick solid line is the overall neutral curve along which helical instability is led either by a $m = -1$ mode ($S \leqslant 1.436$) or a $m = -2$ mode ($S \geqslant 1.436$). The thin dashed lines are the neutral curves pertaining to azimuthal wavenumbers $m = -1$ to $m = -4$, the relevant wavenumber being indicated in the superimposed labels. The thin solid line is the boundary separating the domain of existence of the axisymmetric breakdown solution (light grey shade) from that of the columnar solution, reproduced from figure 3(*b*). The square symbol marks the codimension-two point $S = 1.436$, $Re = 71.95$. (*b*) Variation of the two largest $m = -1$ growth rates when increasing the swirl and keeping the Reynolds number constant and equal to $Re = 164$.

rotational directions are independent of the chosen representation, and it is possible to restrict to azimuthal wavenumbers $m < 0$ with no loss of generality.

3.3. *Mode selection at the threshold of helical instability*

The boundary of the stability domain, shown as the thick solid line in figure 4(*a*), connects 84 neutral points computed in cuts of constant swirl of the (S, Re)-plane. In return, the flow is unstable for combinations of parameters located in the dark grey shade, and stable otherwise. The neutral curves pertaining to each individual wavenumber are also shown as the superimposed thin dashed lines. We find that the transition to helical instability is led either by a $m = -1$ mode ($S < 1.436$) or a $m = -2$ mode ($S > 1.436$). The cross-over point $S = 1.436$, $Re = 71.95$ at which the $m = -1$ and $m = -2$ neutral curves intersect (square symbol in figure 4*a*) is a codimension-two point that will be shown in §§ 5 and 6 to play a key role for selecting the helical pattern observed in the DNSs. Note that higher-order modes become subsequently unstable at large swirl ($S > 1.36$ for $m = -3$, $S > 1.57$ for $m = -4$), consistently with previous results issuing from local stability analyses of model, parallel swirling jets (Lim & Redekopp 1998; Loiseleux, Chomaz & Huerre 1998; Gallaire & Chomaz 2003). In the following, the focus is yet only on the $m = -1$ and $m = -2$ modes, which are those bearing relevance for interpreting the DNS results of Ruith *et al.* (2003), who report synchronized states characterized by either a single helix structure (azimuthal wavenumber $m = -1$, low swirl), or a double helix structure (azimuthal wavenumber $m = -2$, large swirl). The present change in the leading mode is likely to result from the progressive deformation of the axisymmetric breakdown bubble. When increasing the swirl along the neutral curve, we indeed observe the formation of a second corotating bubble, substantially separated from the primary bubble in the axial direction ($S = 1.3$). The secondary bubble extends progressively

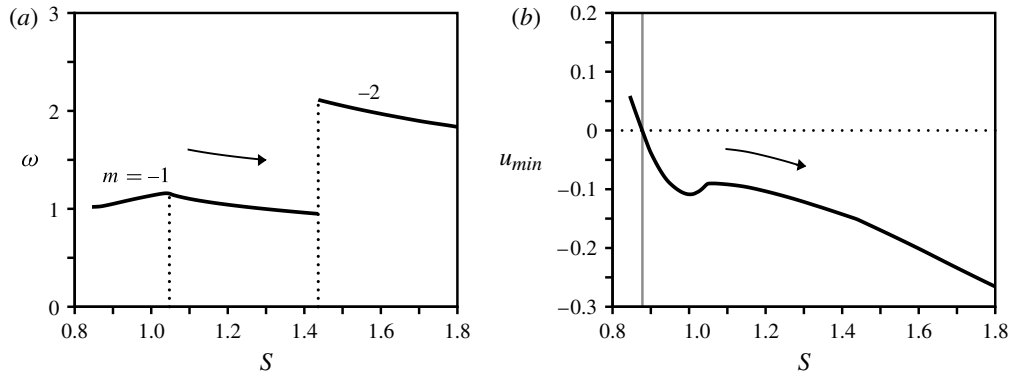

FIGURE 5. (*a*) Variation of the marginal oscillation frequency at the instability threshold, i.e. for parameter couples (S, Re) varying along the neutral curve in figure 4(*a*). The Reynolds number therefore varies from 300 to 40.5 when increasing the swirl following the arrow. The vertical dotted lines mark the swirl values $S = 1.048$ and $S = 1.436$, corresponding respectively to the avoided crossing and to the change in the leading mode. (*b*) Variation of the minimum velocity $w_{0,min}$ defined from (3.1) at the instability threshold. The vertical grey line marks the swirl $S = 0.878$ at which the curve crosses the zero axis, shown by the horizontal dotted line.

further upstream until both bubbles collide ($S \sim 1.4$) and finally merge into a large, deformed bubble ($S = 1.5$, not shown here for conciseness).

Swirling has a dramatic destabilizing effect, since the critical Reynolds number decreases by approximately 85 %, from $Re = 300$ at $S = 0.845$ to $Re = 40.5$ at $S = 1.8$. Note the distortions of the $m = -1$ neutral curve close to the value $S = 1.05$, caused by the avoided crossing of two eigenvalues (Tuckerman 2001). This phenomenon is best seen in figure 4(*b*) showing the evolution of the two largest $m = -1$ growth rates when increasing the swirl and keeping the Reynolds number constant ($Re = 164$, i.e. the critical Reynolds number for $S = 1$). A characteristic cusp behaviour is observed at the value $S = 1.048$ (leftmost vertical dotted line) for which the neutral curve exhibits maximum distortion in figure 4(*a*). The oscillation frequency of the leading mode is shown in figure 5(*a*) at the threshold of instability, i.e. for parameter couples (S, Re) varying along the neutral curve in figure 4(*a*). Values represented on both side of the codimension-two swirl $S = 1.436$ exhibit limited variations ($\omega \sim 1$ for $m = -1$, $\omega \sim 2$ for $m = -2$), although swirling yields a regular, albeit limited, decrease in the frequencies above the threshold of avoided crossing, indicated by the leftmost dotted line.

The axial velocity component of the marginally stable $m = -1$ eigenvector is depicted in figure 6(*a*) for $S = 1$ and $Re = 164$ (real part in the upper half of the plot/imaginary part in the lower half). It indicates that the structure starts developing not in the immediate vicinity of the stagnation point located at $z = 1.3$, but in the lee of the recirculation bubble ($z \sim 4$) where the disturbances amplitude is maximum. It extends further downstream with positive and negative velocity perturbations alternating in a regular, periodic way which allows defining a spatial wavelength of approximately 7 vortex radii. The imaginary part being in advanced spatial quadrature, with extrema located precisely where the real part vanishes, we conclude that this mode is a spiral perturbation rotating in time in the same direction as the swirling flow ($\omega/m < 0$) but winding in space in the opposite direction ($m\varphi > 0$), as observed

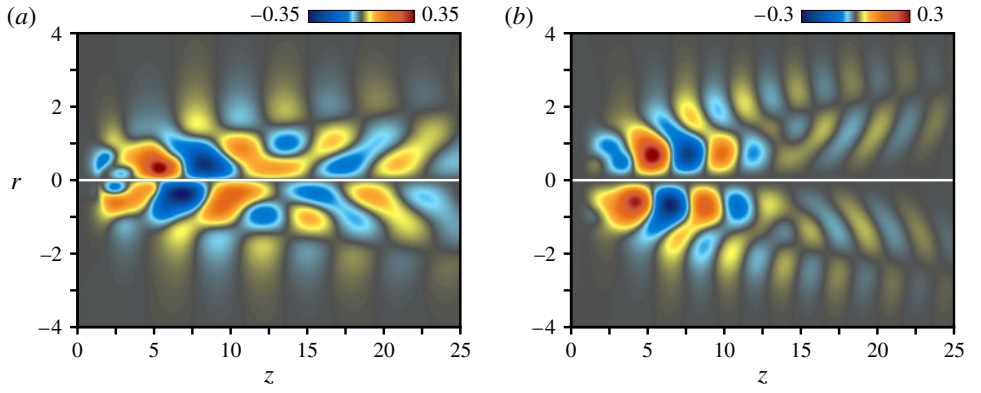

FIGURE 6. (*a*) Spatial distribution of axial velocity for the marginally stable $m = -1$ global mode, $Re = 164$, $S = 1$ (real part in the upper half of the plot/imaginary part in the lower half). (*b*) Same as (*a*) for the marginally stable $m = -2$ global mode, $Re = 69.8$, $S = 1.45$.

in the nonlinear simulations of Ruith *et al.* (2003). Similar results are obtained for the marginally stable $m = -2$ eigenvector (figure 6*b* for $S = 1.45$ and $Re = 69.8$), the only quantitative differences with respect to the $m = -1$ case being that the structure takes its root further downstream and that the local wavelength is shorter by almost 50 % (∼3.5 vortex radii).

The boundary separating the domain of existence of the axisymmetric breakdown solution (light grey shade) from that of the columnar solution is reproduced as the thin solid line in figure 4(*a*). Except at the lowest swirl (and thereby the largest Reynolds numbers), the columnar solution is stable and the helical modes bifurcate from the axisymmetric breakdown solution, which stresses the presence of an axisymmetric bubble as an essential prerequisite to instability. For $S \leqslant 0.878$, no such bubble exists rigourously speaking and the helical modes bifurcate from a columnar solution on the verge of vortex breakdown, as seen from the small, positive values of $w_{0,min}$ computed along the neutral curve and represented in figure 4(*b*). Nonetheless, such swirling wakes with weak coflow at the centreline are known to be absolutely unstable to helical modes (Delbende, Chomaz & Huerre 1998). The present results therefore fully support the interpretation of spiral vortex breakdown in terms of bifurcated states from the axisymmetric breakdown solution.

4. Mode selection above the threshold of helical instability

We address now the question of mode selection above the threshold of helical instability. From now on, the leading $m = -1$ mode is renamed mode A for ease of reading, his amplitude is denoted by A, and all related quantities are denoted correspondingly as ω_A, $\hat{\boldsymbol{q}}_A$, etc. Similar notation is used for the leading $m = -2$ mode, renamed mode B. To avoid confusion, all quantities evaluated at threshold of instability are denoted by the subscript c.

4.1. *The single helix at* $S = 1$

We set here the swirl to the value $S = 1$ and use the Reynolds number as the only variable parameter. The linear stability analysis has assessed that mode A becomes unstable through a Hopf bifurcation at the critical Reynolds number $Re_{cA} = 164$. At $Re = 200$, mode A is the only unstable $m = -1$ mode, as seen from the eigenvalue

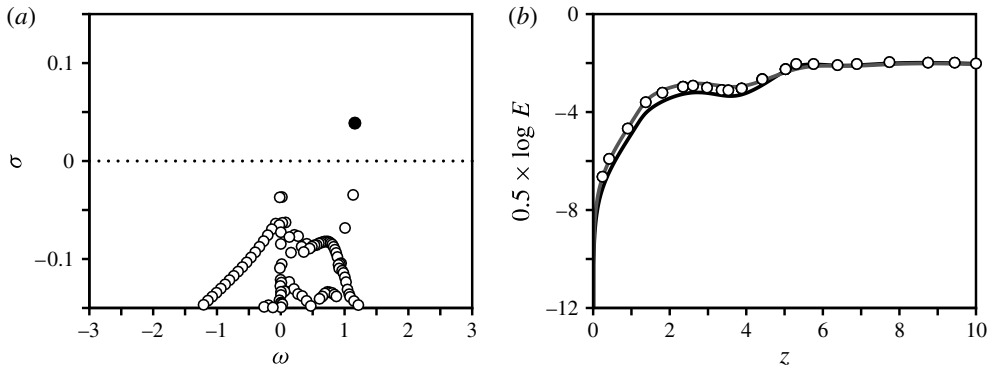

FIGURE 7. (*a*) Eigenvalue spectrum in the (ω, σ)-plane for modes of azimuthal wavenumber $m = -1$, $Re = 200$, $S = 1$. (*b*) Radially averaged energy distribution $E(z)$ defined by (4.1) for the unstable $m = -1$ mode at $Re = 200$, $S = 1$. The black line corresponds to the saturated energy of the first-order solution, reconstructed from the Stuart–Landau equation (4.2). The grey line corresponds to the conveniently normalized energy of the linear global mode. The circle symbols correspond to the $m = -1$ Fourier mode extracted from a fully nonlinear DNS by Gallaire *et al.* (2006).

	LGS	NLGS	Fronts	DNS
σ_A	0.0387	—	—	0.0359
ω_A	1.16	1.22	1.25	1.18

TABLE 1. Stability properties of the single helix at $Re = 200$, $S = 1$. The growth rate and frequency of mode A issuing from the present linear global stability (LGS) and nonlinear global stability (NLGS) analyses are provided in columns 2 and 3. Results obtained using the nonlinear fronts theory of weakly non-parallel flows (Gallaire *et al.* 2006) are reported for comparison in column 4. Data issuing from the DNSs of Ruith *et al.* (2003) are provided in column 5, the growth rate being measured from the transient, and the frequency from the saturated limit cycle behaviour.

spectrum presented in figure 7(*a*) where mode A is indicated by the filled symbol. In addition, all other $m = -2$ and higher-order modes are stable (not shown in the figure), consistently with the DNS calculations of Ruith *et al.* (2003) who report a $m = -1$ instability and the emergence of a single helix at the same parameter settings. As seen in table 1, there is a good agreement between the growth rate predicted by the present linear global analysis and the growth rate extracted by these authors from the initial transient of their initially axisymmetric nonlinear simulations. The frequency prediction relative to precessing rotation $\omega_A = 1.16$ of the structure is also excellent, when compared with the value $\omega \sim 1.18$ extracted from the nonlinear limit cycle. The agreement is even more accurate than the value 1.22 issuing from the weakly non-parallel analysis performed by Gallaire *et al.* (2006).

The spatial structure of the unstable mode is reminiscent of that depicted in figure 6(*a*) at threshold of instability. The axial evolution of the radially averaged

energy density defined by

$$E(z) = 2\pi \int_0^{r_{max}} \frac{1}{2} |\hat{\boldsymbol{u}}|^2 \, r \, \mathrm{d}r, \tag{4.1}$$

is displayed by the black line in figure 7(*b*). Since the normalization of linear global modes is arbitrary, all magnitudes have been rescaled for the total energy integrated in the axial direction to be equal to 0.333, a choice which might seem odd *a priori*, but will come out naturally in the following. Interestingly, the disturbances energy grows from the inlet in two successive stages, the first one in the region $z \leqslant 3$ and the second one in the region $z \geqslant 4$. A similar feature has been reported for the energy of the nonlinear $m = -1$ Fourier mode extracted from the DNSs, and attributed to the existence of two absolutely unstable regions (Gallaire *et al.* 2006, see the figure 7 herein). The data points provided by these authors have been appropriately rescaled since originally presented in terms of an energy per unit volume of the computational domain, and reported as the circle symbols in figure 7(*b*). Both data sets exhibit a very good agreement, hence suggesting that the exact 3D solution can be approximated with reasonable accuracy by superposing the axisymmetric breakdown state and the unstable mode A with appropriate amplitude.

Quantitative predictions can be obtained from the normal form, which reduces here to the Stuart–Landau amplitude equation for A reading

$$\mathrm{d}_t A = \alpha_A \left(\frac{1}{Re_{cA}} - \frac{1}{Re} \right) A - \mu_A A \, |A|^2, \tag{4.2}$$

since we recall that the Reynolds number is the only variable parameter. In (4.2) α_A accounts for the linear variation of the eigenvalue when the Reynolds number departs from criticality. In contrast, μ_A is the Landau coefficient governing the nonlinear saturation of the amplitude, which can be shown to stem from two distinct origins at play at second order in the expansion, namely the mean-flow correction generated by the development of the unstable mode A, and the growth of the first harmonic which corresponds here a spiral wave of azimuthal wavenumber $m = -2$ precessing at the frequency $2\omega_{cA}$. Using the analytical expressions provided in appendices A and B, we obtain numerically

$$\alpha_A = 28.1 + 21.8\mathrm{i}, \quad \mu_A = 0.545 - 1.63\mathrm{i}, \tag{4.3}$$

and find that the contribution of the mean-flow correction to the Landau coefficient dominates by one order of magnitude over that of the first harmonics ($0.482 - 1.56\mathrm{i}$ versus $0.0633 - 0.067\mathrm{i}$). Physically, this means that disturbances saturate beyond the threshold of instability because the mean-flow correction modifies the steady base flow in a stabilizing manner.

The amplitude of the single helix, i.e. the limit cycle solution of (4.2), is known analytically as $A = |A| \exp(\mathrm{i}\omega_A t)$, with

$$|A|^2 = \frac{\alpha_{Ar}}{\mu_{Ar}} \left(\frac{1}{Re_{cA}} - \frac{1}{Re} \right), \tag{4.4a}$$

$$\omega_A = \omega_{cA} + \alpha_{Ai} \left(\frac{1}{Re_{cA}} - \frac{1}{Re} \right) - \alpha_{Ar} \frac{\mu_{Ai}}{\mu_{Ar}} \left(\frac{1}{Re_{cA}} - \frac{1}{Re} \right). \tag{4.4b}$$

It can be inferred that the precession frequency computed from (4.4*b*) is lower than the value predicted solely by the stability analysis, on account of the nonlinear correction proportional to $\mu_{Ai} > 0$. For $Re = 200$, we obtain a value $\omega_A = 1.25$ ($\omega_{cA} = 1.13$)

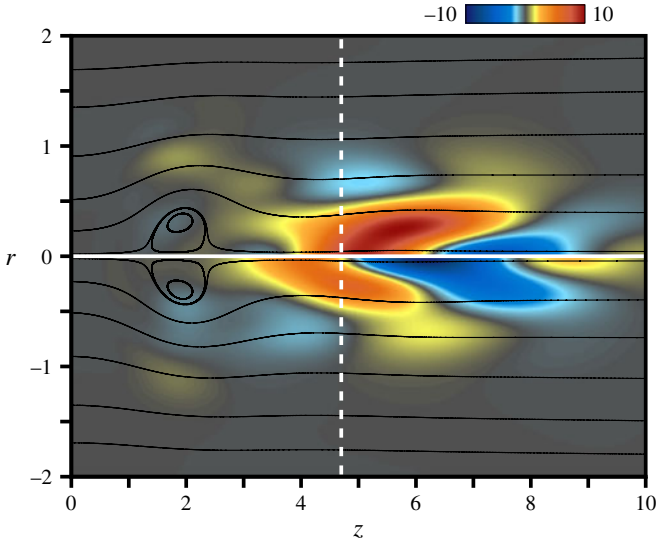

FIGURE 8. Spatial distribution of the coupling density field $\mu_A(r, z)$ at $Re = 164$, $S = 1$ (real part in the upper half of the plot/imaginary part in the lower half), along with the streamlines of the axisymmetric breakdown solution.

consistent with the saturated limit cycle frequency measured from the DNSs (Gallaire *et al.* 2006). The radially averaged energy density of the first-order solution has been computed for the corresponding amplitude $|A| = 0.237$, the energy integrated in the axial direction being then 0.333, i.e. precisely that obtained from the linear amplitude normalized above. The nonlinear results are therefore presented without any rescaling as the grey line in figure 7(*b*). The agreement with the fully nonlinear structure reported from Gallaire *et al.* (2006) is excellent, even better than in the linear case, which demonstrates that only weakly nonlinear mechanisms are at play. In return, the dynamics of the exact 3D fully nonlinear solution is accurately predicted by the normal form.

The consistency between our weakly nonlinear, fully non-parallel analysis and its fully nonlinear, weakly non-parallel counterpart (Gallaire *et al.* 2006) is to be emphasized. As an attempt to carry the comparison still further, we introduce the density field $\mu_A(r, z)$ defined such that $\mu_A = \int_\Sigma \mu_A(r, z) r \, \mathrm{d}r \, \mathrm{d}z$, whose analytical expression is provided in appendix A. Its spatial distribution is represented in figure 8, where we have superimposed the streamlines of the underlying axisymmetric breakdown solution. Interestingly, the density is negligible in the inner breakdown bubble and significant only in its lee ($4 \leqslant z \leqslant 8$). This is the specific nonlinear feedback region where happen all nonlinear interactions governing the saturation of the single helix. This localization is fully consistent with the position $z = 4.7$ of the nonlinear wavemaker reported by Gallaire *et al.* (2006) using the theory of nonlinear fronts (vertical dashed line in figure 8). Nonetheless, such an agreement relies on no theoretical background and is thus not further explained here.

4.2. *The single and double helices at* $S = 1.3$

We set now the swirl to the value $S = 1.3$, for which the linear stability analysis has assessed that modes A and B become successively unstable through Hopf bifurcations

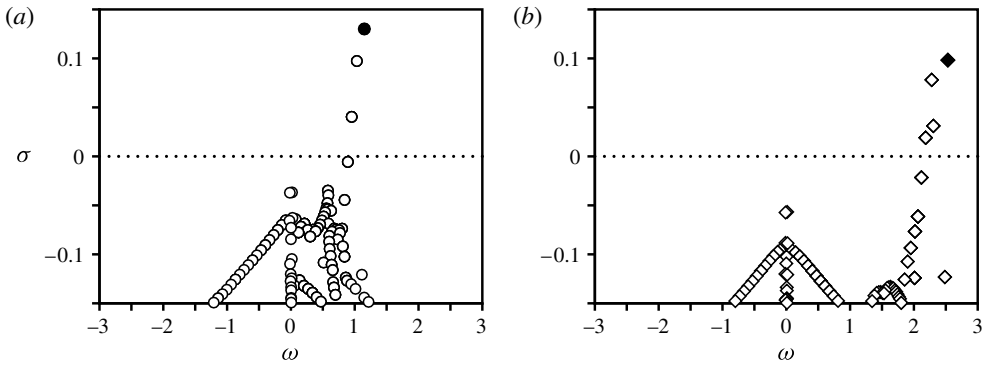

FIGURE 9. Eigenvalue spectra in the (ω, σ)-plane for modes of azimuthal wavenumbers (a) $m = -1$ and (b) $m = -2$, $Re = 200$, $S = 1.3$.

Re	S	LGS mode A	LGS mode B	Transient DNS $m = -1$	Transient DNS $m = -2$	DNS limit cycle
120	1.3	0.0645	−0.000761	0.0476	Stable	$m = -1$
150	1.3	0.103	0.0339	0.0843	0.00850	$m = -2$
200	1.3	0.129	0.0974	0.110	0.0674	$m = -2$

TABLE 2. Synoptic table of the stability properties at $S = 1.3$: the growth rates of modes A and B issuing from the present linear global stability (LGS) analyses are provided in columns 3 and 4. Data issuing from the DNSs of Ruith *et al.* (2003) are reported for comparison: the dominant growth rates measured from the transient are provided in columns 5 and 6, and the azimuthal wavenumber of the saturated limit cycle behaviour is provided in column 7.

at respective Reynolds numbers $Re_{cA} = 87.7$ and $Re_{cB} = 120.7$. At $Re = 200$, several unstable modes coexist, as seen from the eigenvalue spectra represented in figure 9, modes A and B being the dominant modes indicated by the filled symbols. The corresponding growth rates provided in table 2 are consistent with those extracted by Ruith *et al.* (2003) from the dynamics of initially axisymmetric simulations. Discrepancies however exist, that can be explained in two different ways.

(i) Both studies significantly differ by the employed spatial resolution, namely we use ∼550 000 grid points distributed over a single azimuthal plane, whereas Ruith *et al.* (2003) used ∼700 000 grip points distributed over 61 azimuthal planes, or equivalently ∼11 000 points per plane.

(ii) In the DNS, growth rates are identified from the time evolution of disturbances integrating all azimuthal wavenumbers. In return, the simultaneous existence of several unstable modes yields a distorted exponential behaviour (see, for instance, figure 28 in Ruith *et al.* 2003) and yields limited accuracy compared to the present eigenvalue calculations converged down to the third digit, as evidenced in appendix E.

Since mode A has the largest growth rate over all possible disturbances, a single helix pattern should emerge in the DNSs, but Ruith *et al.* (2003) report the saturation of a double helix. Similar results are obtained for $Re = 150$, even though the growth

rate of mode B is thrice as small as that of mode A. Conversely, the single helix is recovered for $Re = 120$, as mode B is then incipiently stable. These results clearly stress that mode selection does not proceed from a linear mechanism at parameter settings where modes A and B are simultaneously unstable, since the usual 'first to bifurcate' and 'largest growth rate' criteria neither explain, nor predict the mode selection observed in the DNSs. Repeating the nonlinear analysis documented in § 4.1 is susceptible to give insight into some aspects of the flow physics but only little improvement is to be expected. Indeed, the Reynolds number is the only variable parameter, and the normal form reduces to a system of Stuart–Landau equations

$$\mathrm{d}_t A = \alpha_A \left(\frac{1}{Re_{cA}} - \frac{1}{Re} \right) A - \mu_A A \left| A \right|^2, \tag{4.5a}$$

$$\mathrm{d}_t B = \alpha_B \left(\frac{1}{Re_{cB}} - \frac{1}{Re} \right) B - \mu_B B \left| B \right|^2, \tag{4.5b}$$

allowing investigating the nonlinear behaviours only in subspaces restricted to the azimuthal wavenumber of each individual mode. In other words, we can describe the single helix (limit cycle of (4.5*a*)) and the double helix (limit cycle of (4.5*b*)) separately, but we cannot describe the coupling between them. Even so, we have computed the coefficients of the normal form and checked that both modes have comparable saturation time scales and amplitudes. This contrasts with the unambiguous observation of a double helix in the DNSs, and stresses the need for a more consistent analysis.

5. Mode selection via the double-Hopf interaction

Assuming that both the swirl and the Reynolds numbers are now variable parameters, we compute the dynamics near the codimension-two point, i.e. the critical swirl and Reynolds numbers from now on are $S_c = 1.436$ and $Re_c = 71.95$. The normal form describing this double-Hopf interaction is given by

$$\mathrm{d}_t A = \lambda_A A - \mu_A A \left| A \right|^2 - \nu_A A \left| B \right|^2, \tag{5.1a}$$

$$\mathrm{d}_t B = \lambda_B B - \mu_B B \left| B \right|^2 - \nu_B B \left| A \right|^2 . \tag{5.1b}$$

It differs from (4.5) by two coupling terms stemming from third-order nonlinearities, namely the term $\nu_A A \left| B \right|^2$ in equation (5.1*a*) for A and the symmetric term $\nu_B B \left| A \right|^2$ in equation (5.1*b*) for B, and is formally identical to that used by other authors to describe the bifurcation sequence undergone in various swirling flow configurations (Marques, Lopez & Shen 2002; Marques, Gelfgat & Lopez 2003; Nore *et al.* 2003; Abshagen *et al.* 2005; Nore, Moisy & Quartier 2005; Avila, Meseguer & Marques 2006; Lopez 2006), although our situation differs by the instability mechanisms at hand and by the method used to derive the normal form itself. We show in appendix A that the linear coefficients can be expressed as

$$\lambda_A = \alpha_A \left(\frac{1}{Re_c} - \frac{1}{Re} \right) + \beta_A (S_c - S), \tag{5.2a}$$

$$\lambda_B = \alpha_B \left(\frac{1}{Re_c} - \frac{1}{Re} \right) + \beta_B (S_c - S), \tag{5.2b}$$

where the additional terms β_A and β_B account for the linear variation of the eigenvalues when the swirl departs from criticality. We provide here the numerical

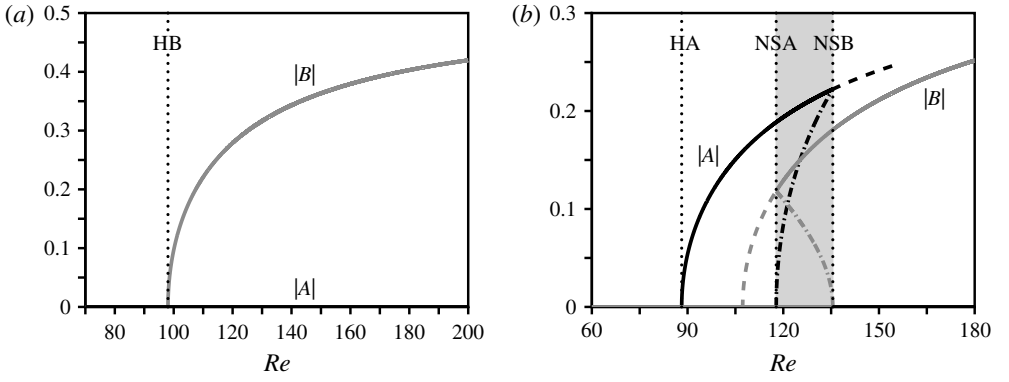

FIGURE 10. (*a*) Amplitude of the bifurcating modes as a function of the Reynolds number, as predicted by the normal form (5.1) for $S = 1.5$. The vertical dotted line marks the occurrence of the first Hopf bifurcation at $Re_{HB} = 62.4$. (*b*) Same as (*a*) for $S = 1.3$. The vertical dotted lines mark the occurrence of the first Hopf bifurcation at $Re_{HA} = 88.2$ and that of the secondary and tertiary Neimark–Sacker bifurcations at $Re_{NSB} = 135.5$ and $Re_{NSA} = 117.8$. The amplitudes of modes A and B are represented by the various black and grey lines, respectively. The stable and unstable parts of the pure solutions are shown by the solid and dashed lines, respectively, and the unstable T2 torus solution by the dash-dotted lines. The light grey shade indicates the domain $[Re_{NSA}; Re_{NSB}]$ where the system is hysteretic.

value of the coefficients

$$\left.\begin{aligned} \alpha_A &= 15.0 + 12.3\mathrm{i}, & \alpha_B &= 14.1 + 28.1\mathrm{i}, \\ \beta_A &= -0.282 + 0.112\mathrm{i}, & \beta_B &= -0.472 + 0.0963\mathrm{i}, \\ \mu_A &= 1.20 + 0.198\mathrm{i}, & \mu_B &= 0.836 - 1.07\mathrm{i}, \\ \nu_A &= 3.06 - 0.995\mathrm{i}, & \nu_B &= 0.553 - 0.548\mathrm{i}, \end{aligned}\right\} \tag{5.3}$$

and postpone to § 7 the discussion of their physical origin.

5.1. *Bifurcation diagrams*

The general theory of double-Hopf bifurcations has been elaborated on (Guckenheimer & Holmes 1983) and many dynamical behaviours are known to arise (see Kuznetsov 1998, for a comprehensive description). We only mention here that the present normal form with analytically computed coefficients pertains to the so-called simple case ($\mu_{Ar}\mu_{Br} > 0$), and discuss only the solutions relevant to our problem which turn to be known analytically. The stability of all solutions has been assessed by time-marching equations (5.1) using a fourth-order Runge–Kutta scheme and checked using the AUTO continuation software (Doedel *et al.* 1997).

The bifurcation diagram presented in figure 10(*a*) for $S = 1.5$ exhibits a single bifurcation at $Re_{HB} = 62.4$, where mode B bifurcates from the axisymmetric breakdown solution (Hopf bifurcation denoted HB). Saturation of the amplitude gives rise to a pure double helix which subsequently remains the only stable solution. Note that the threshold value slightly departs from that $Re = 62.9$ issuing from the linear stability analysis, since the normal form does not use the computed growth rates of the individual global modes, but only an approximation linearized at the codimension-two point.

In contrast, the bifurcation diagram presented in figure 10(*b*) for $S = 1.3$ exhibits a complex series of bifurcations. Mode A bifurcates first from the axisymmetric breakdown solution at $Re_{HA} = 88.2$ (Hopf bifurcation HA), which gives rise to a single helix (black solid line). Mode B then bifurcates from the single helix at $Re_{NSB} = 135.5$ (Neimark–Sacker bifurcation NSB, also called a Hopf bifurcation of the first return map of the limit cycle), hence yielding a quasi-periodic T2 torus on which both modes oscillate with finite amplitudes and incommensurate frequencies (dash–dotted lines in figure 10*b*). This torus is the saturated limit cycle for the coupled system (5.1), whose amplitudes are known analytically as $|A|\exp(\mathrm{i}\omega_A t)$ and $|B|\exp(\mathrm{i}\omega_B t)$ with

$$|A|^2 = \frac{\lambda_{Ar}\mu_{Br} - \nu_{Ar}\lambda_{Br}}{\mu_{Ar}\mu_{Br} - \nu_{Ar}\nu_{Br}}, \tag{5.4a}$$

$$|B|^2 = \frac{\mu_{Ar}\lambda_{Br} - \lambda_{Ar}\nu_{Br}}{\mu_{Ar}\mu_{Br} - \nu_{Ar}\nu_{Br}}, \tag{5.4b}$$

$$\omega_A = \omega_{cA} + \lambda_{Ai} - \lambda_{Ar}\frac{\mu_{Ai}\mu_{Br} - \nu_{Ai}\nu_{Br}}{\mu_{Ar}\mu_{Br} - \nu_{Ar}\nu_{Br}} - \lambda_{Br}\frac{\mu_{Ar}\nu_{Ai} - \mu_{Ai}\nu_{Ar}}{\mu_{Ar}\mu_{Br} - \nu_{Ar}\nu_{Br}}, \tag{5.4c}$$

$$\omega_B = \omega_{cB} + \lambda_{Bi} - \lambda_{Br}\frac{\mu_{Ar}\mu_{Bi} - \nu_{Ar}\nu_{Bi}}{\mu_{Ar}\mu_{Br} - \nu_{Ar}\nu_{Br}} - \lambda_{Ar}\frac{\mu_{Br}\nu_{Bi} - \mu_{Bi}\nu_{Br}}{\mu_{Ar}\mu_{Br} - \nu_{Ar}\nu_{Br}}. \tag{5.4d}$$

The subcritical nature of the NSB bifurcation, clearly visible from the present analytical amplitudes, imposes the torus solution to be unstable. Nonetheless, the latter torus plays a fundamental role in the dynamics by leading the emergence of the double helix (grey solid line) through a second Neimark–Sacker bifurcation (NSA) at $Re_{NSA} = 117.8$, best understood in terms of the backward bifurcation of mode A from the double helix. On behalf of subcriticality, the system is hysteretic in the range $Re_{NSA} \leqslant Re \leqslant Re_{NSB}$ where either the single or the double helices can emerge from random initial conditions, which has been ascertained from our Runge–Kutta simulations.

5.2. *Mode selection*

Computation of the above bifurcation diagrams can be repeated for any value of the swirl in order to build a map of the solutions observed in the (S, Re)-plane. The general picture outlined above is confirmed, with either the only stable double helix at swirl $S > S_c$, or the stable single and double helices connected through an unstable torus at swirl $S < S_c$. The obtained results are synthesized in figure 11, where we report four distinct domains branching at the codimension-two point (square symbol), and corresponding respectively to the axisymmetric breakdown solution (white shade labelled 0), the single helix (black shade labelled H1), the double helix (dark grey shade labelled H2) and the hysteretic domain where the single and double helices coexist (light grey shade). We also report in figure 11 data points documented by Ruith *et al.* (2003) for $S = 1.3$ (open circle for the single helix prevailing at $Re = 120$, open diamond for the double helix prevailing at $Re = 150$), seen to match remarkably well the predictions of the normal form (table 2).

The bifurcated single helix found at $Re = 120$ is illustrated in figure 12(*a*) depicting the isosurface of azimuthal vorticity $\xi = -1.15$ of the second-order analytic solution reconstructed from the asymptotic expansion, as explained in appendix A. An alternative representation is proposed in figure 12(*b*), which simulates an experimental dye visualization and shows numerically computed dye lines transported at $t = 70$ by the same analytic solution. Such visualization has been obtained by initially releasing

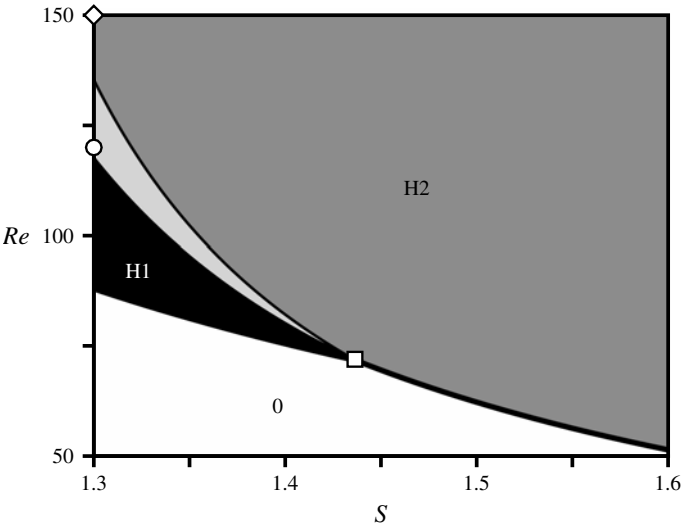

FIGURE 11. Map of the nonlinear patterns in the (S, Re)-plane, as predicted by the normal form (5.1). The axisymmetric breakdown state prevails in the white shade labelled 0. The single helix and the double helix prevail in the black and dark grey shades labelled H1 and H2, respectively, the hysteresis range being indicated by the light grey shade. The square symbol marks the codimension-two point. The symbols at $S = 1.3$ correspond to parameter values documented by Ruith *et al.* (2003) (circle if the DNS predicts a single helix, diamond if it predicts a double helix).

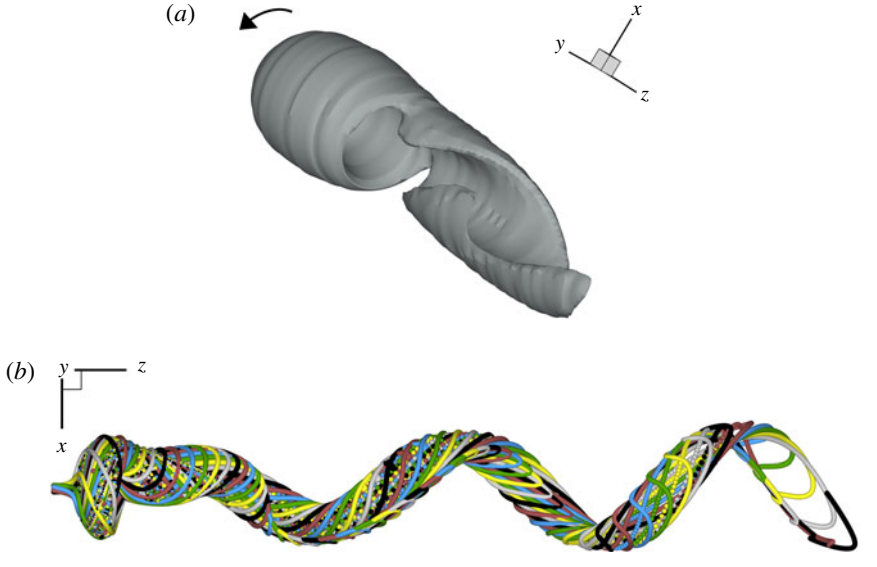

FIGURE 12. (Colour online available at journals.cambridge.org/flm) Visualization of the stable simple helix at $Re = 120$, $S = 1.3$, based on the second-order analytic solution reconstructed from (5.1). (*a*) Isosurface of azimuthal vorticity $\xi = -1.15$. The black arrow indicates the swirling direction of the ambient flow. (*b*) Numerically computed dye lines at $t = 70$ (see supplementary movie 1 for an animation). In (*b*), the scale is doubled in the axial direction.

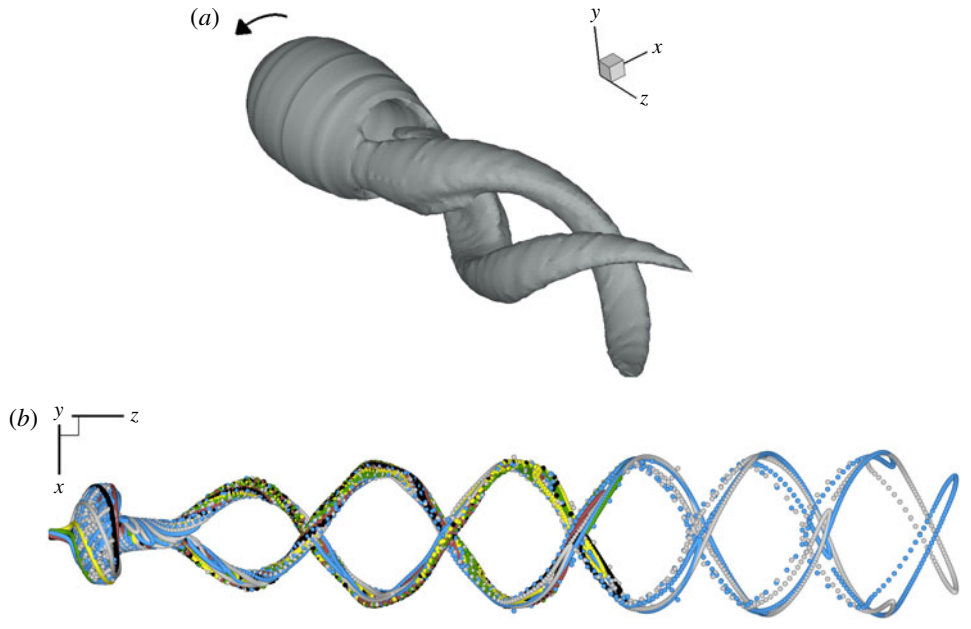

FIGURE 13. (Colour online) Same as figure 12 for the stable double helix at $Re = 150$, $S = 1.3$; see supplementary movie 2 for an animation.

particles at six equidistant azimuthal positions at the inlet, close to the axis ($r = 0.05$). Note the agreement with the fully nonlinear structure documented by Ruith *et al.* (2003) (see figure 20 herein). In particular, the winding and rotational directions observed in the DNSs are retrieved, this being more clearly perceived from viewing the accompanying supplementary movie 1 available at journals.cambridge.org/flm. The bifurcated double helix found at $Re = 150$, illustrated in a similar manner in figure 13 (isosurface of vorticity $\xi = -1.15$ and numerical dye lines at $t = 70$), also reproduces accurately the fully nonlinear solution of Ruith *et al.* (2003). Additional visualizations of the torus are provided in figure 14, although this flow is unstable and should not be observed in practice. Results indicate that only the double helical component is detected in the near wake, whereas the single helical component is best seen in the far wake owing to the difference in the spatial extent of the respective modes.

6. Mode selection via the double-Hopf interaction with 2:1 resonance

We complement here the previous analysis by deriving an alternative normal form encompassing the fact that the system is close to a strong 2:1 resonance at the codimension-two bifurcation point, since the marginal frequencies $\omega_{cA} = 0.949$ and $\omega_{cB} = 2.113$ are such that $\omega_{cB}/\omega_{cA} \sim 2$. In return, phase locking between modes may occur and enrich the dynamics. Note that the approach is relevant even though the 2:1 resonance is only approximately satisfied, since the amplitude of a marginally stable global mode of frequency ω, forced at a frequency ω_f, is proportional to $1/|\omega - \omega_f|$.

The normal form describing this interaction is given by

$$\mathrm{d}_t A = \lambda_A A - \mu_A A\,|A|^2 - \nu_A A\,|B|^2 - \eta A^* B, \tag{6.1a}$$

$$\mathrm{d}_t B = \lambda_B B - \mu_B B\,|B|^2 - \nu_B B\,|A|^2 - \chi A^2, \tag{6.1b}$$

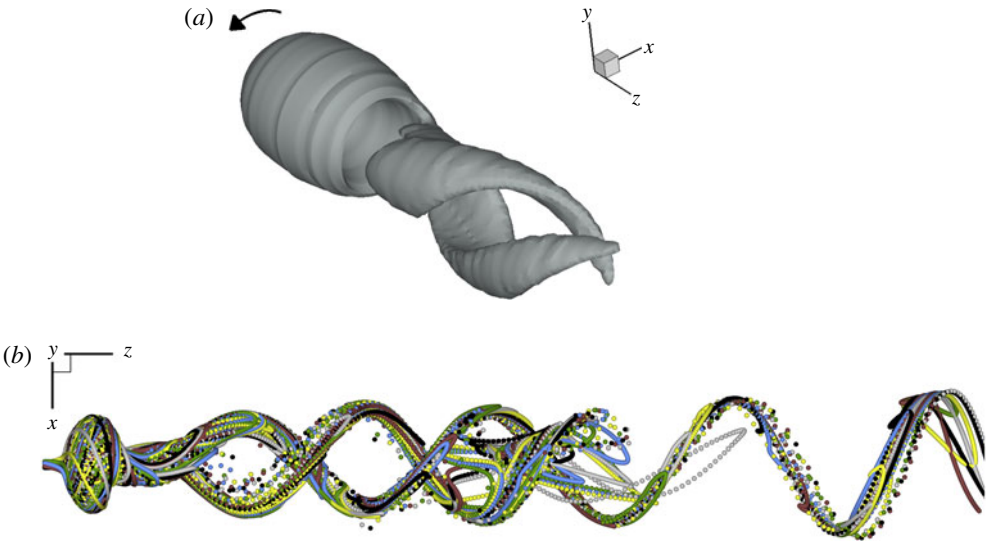

FIGURE 14. (Colour online) Same as figure 12 for the unstable T2-torus at $Re = 120$, $S = 1.3$; see supplementary movie 3 for an animation.

and differs from (5.1) by two terms linked to subharmonic resonances, namely the quadratic harmonic forcing term χA^2 in equation (6.1*b*) for B and the harmonic feedback $\eta A^* B$ in equation (6.1*a*) for A. Both are due to second-order nonlinearities and are unusual compared with the coefficients ν_A and ν_B introduced in § 5 to describe the classical interaction between non-resonant modes.

We compute all coefficients in (6.1) applying the formalism of a double Hopf bifurcation with exact 2:1 resonance, which in the present case is of codimension-three. It is feasible to compute the exact codimension-three point by adding in a third variable parameter, for instance that introduced by Grabowski & Berger (1976) to control the ratio of the centreline to free stream axial velocities. We choose an alternative approach consisting in assuming a small detuning between modes and in staying in our two-parameter plane, seen as a cut through the unfolding of the nearby codimension-three bifurcation. For the formalism to apply, we resort to the shift technique introduced in Meliga, Chomaz & Sipp (2009), which allows correcting selected eigenvalues of a linear operator with no change in the associated eigenmodes. All relevant details are provided in appendix A, where we show that the marginal frequencies ω_{cA} and ω_{cB} are replaced in the numerics by the shifted frequencies ω_{res} and $2\omega_{res}$ defined from

$$\omega_{res} = \frac{2\omega_{cA} + \omega_{cB}}{4} = 1.003, \tag{6.2}$$

where ω_{res} is the linear approximation of the marginal frequency prevailing at the codimension-three point. We also show in appendix A that the linear coefficients are now split into

$$\lambda_A = \alpha_A \left(\frac{1}{Re_c} - \frac{1}{Re} \right) + \beta_A (S_c - S) + \mathrm{i}\,(\omega_{cA} - \omega_{res})\,, \tag{6.3a}$$

$$\lambda_B = \alpha_B \left(\frac{1}{Re_c} - \frac{1}{Re} \right) + \beta_B (S_c - S) + \mathrm{i}\,(\omega_{cB} - 2\omega_{res})\,, \tag{6.3b}$$

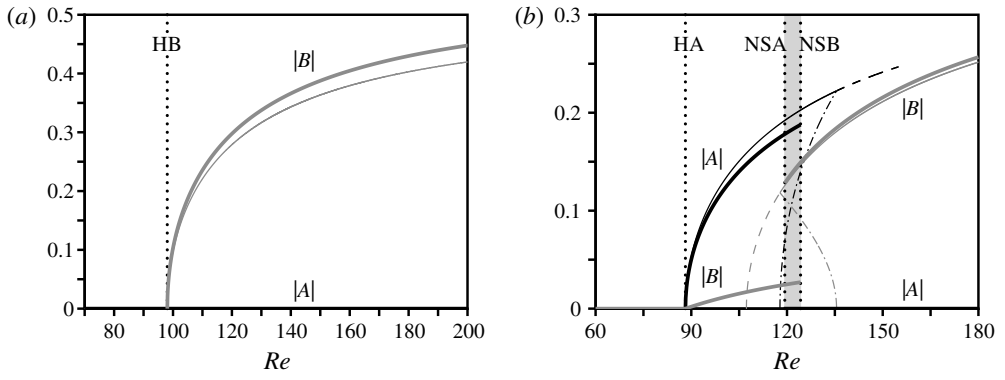

FIGURE 15. Same as figure 10, the amplitudes being now predicted by the normal form (6.1). For both plots, numerical values predicted by the non-resonant normal form (5.1) are also reproduced from figure 10 as finer lines with identical graphic conventions.

where the third term is an offset resulting from the frequency shift procedure, which allows ω_{cA} and ω_{cB} to be recovered as the true marginal frequencies. Numerically, we obtain

$$\left.\begin{array}{ll} \alpha_A = 15.0 + 12.3\mathrm{i}, & \alpha_B = 14.1 + 28.1\mathrm{i}, \\ \beta_A = -0.282 + 0.112\mathrm{i}, & \beta_B = -0.472 + 0.0963\mathrm{i}, \\ \mu_A = 1.30 - 0.269\mathrm{i}, & \mu_B = 0.804 - 1.08\mathrm{i}, \\ \nu_A = 2.70 - 0.921\mathrm{i}, & \mu_B = 0.602 - 0.0335\mathrm{i}, \\ \eta = 0.112 + 0.308\mathrm{i}, & \chi = -0.0292 + 0.164\mathrm{i}, \end{array}\right\} \tag{6.4}$$

the small variations in the values of the nonlinear coefficients compared with (5.3) being an indirect consequence of the frequency shift method, as further explained in appendix A.

6.1. *Bifurcation diagrams*

An exhaustive description of the generic solutions to system (6.1) can be found in Knobloch & Proctor (1988) and LeBlanc & Langford (1996). In the following, we discuss only the solutions relevant to our problem, obtained using `AUTO`.

The bifurcation diagram obtained for $S = 1.5$ is shown in figure 15(a). It is almost identical to that obtained in the non-resonant case (reproduced from figure 10a as the finer grey line), in particular, the threshold value $Re_{HB} = 62.4$ at which the solution bifurcates to the double helix is identical in both cases since determined only from the linear coefficients of the normal form. The bifurcation diagram obtained for $S = 1.3$ is shown in figure 15(b). The first bifurcation threshold $Re_{HA} = 88.2$ is also identical to its non-resonant counterpart (same argument as above), but the nature of the bifurcated state differs, as the single helix is replaced by a mixed-modes solution (A, B) where both amplitudes grow steadily with the Reynolds number. Indeed, the single helix is not a solution of (6.1), where any small but finite amplitude of mode A forces the growth of B through the harmonic term χA^2 in (6.1b). This is illustrated in figure 16 where we present the time evolution of the amplitudes obtained from a simulation of the weakly perturbed trajectories around the trivial solution at $Re = 120$. Both modes are unstable at this Reynolds number, so that their amplitudes grow first exponentially,

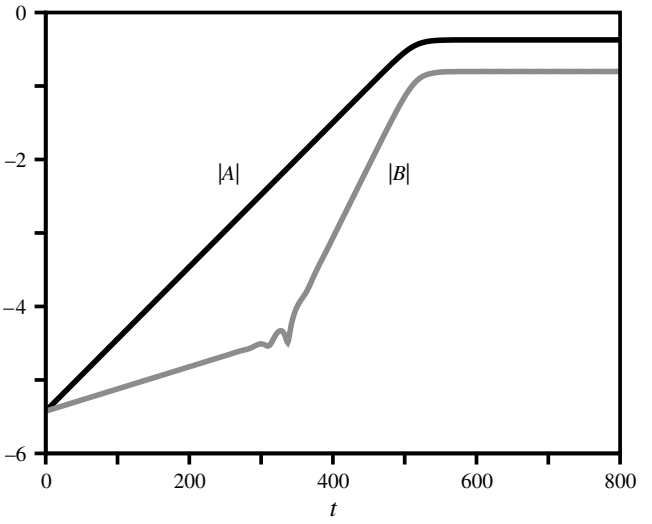

FIGURE 16. Time evolution of the amplitudes obtained from numerical simulations of system (6.1) at $Re = 120$ (logarithmic scale on the vertical axis).

the slope for each mode being given by the individual linear growth rates, thus smaller for B than for A. Only when mode A has reached a sufficient magnitude does the resonance force convergence to the mixed-modes solution, which is seen to occur here at $t \sim 300$. At this stage, the growth rate of B brutally changes to reach roughly twice that of A, mode B being then slaved to the resonant term χA^2. Finally, the solution bifurcates to an unstable torus yielding the emergence of the double helix through subcritical Neimark–Sacker bifurcations at Reynolds numbers $Re_{NSB} = 124.2$ and $Re_{NSA} = 119.3$, the range of Reynolds number sustaining hysteresis (grey shade in figure 15*b* being here reduced compared with that obtained in the non-resonant case). Note that there exist analytical expressions neither for the mixed-modes solution nor for the torus, in contrast to the non-resonant case. Because we could not manage to obtain the torus branches from `AUTO`, subcriticality has thus been carefully ascertained simulating weakly perturbed trajectories around the limit cycle of the mixed-modes solution.

The mixed-modes solution and the unstable torus are not to be confused, although they constitute both limit cycles and involve both non-zero amplitudes A and B. While the torus involves two incommensurate oscillation frequencies, the frequency of mode B is tuned to twice the frequency of A on the mixed-modes solution, which is thus an equilibrium point of the equivalent 3D polar system for $|A|$, $|B|$ and $\phi = 2\arg A - \arg B$, reading

$$\mathrm{d}_t|A| = \lambda_{Ar}|A| - \mu_{Ar}\,|A|^3 - \nu_{Ar}|A|\,|B|^2 - |\eta||A||B|\cos(\phi - \arg\eta), \tag{6.5a}$$

$$\mathrm{d}_t|B| = \lambda_{Br}|B| - \mu_{Br}\,|B|^3 - \nu_{Br}|B|\,|A|^2 - |\chi|\,|A|^2\cos(\phi + \arg\chi), \tag{6.5b}$$

$$\mathrm{d}_t\phi = 2\lambda_{Ai} - \lambda_{Bi} - (2\mu_{Ai} - \nu_{Bi})\,|A|^2 - (2\nu_{Ai} - \mu_{Bi})\,|B|^2 + 2|\eta||B|\sin(\phi - \arg\eta) + |\chi|\frac{|A|^2}{|B|}\sin(\phi + \arg\chi). \tag{6.5c}$$

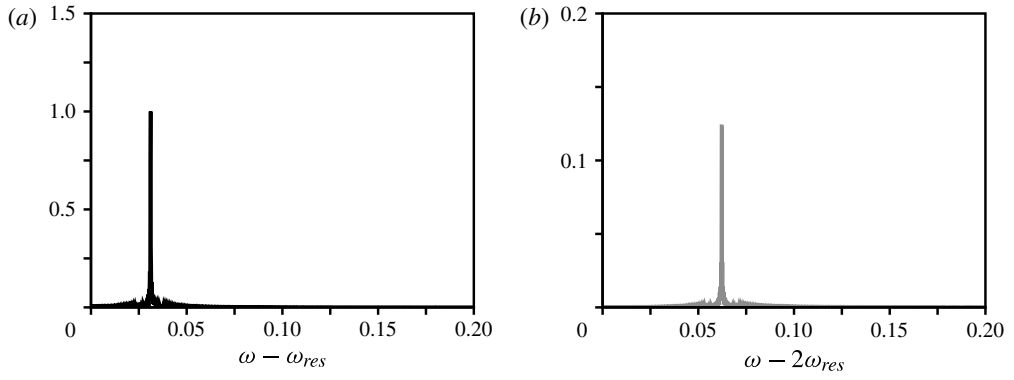

FIGURE 17. Spectra of the amplitude time-series data for $Re = 120$ for (a) mode A and (b) mode B. For both plots, arbitrary units are used on the vertical axis.

This is illustrated in figure 17, showing the results of a standard Fourier transform of the time-series data recorded at $Re = 120$ (here, only the real parts of the complex amplitudes have been retained and processed). One sees that the signals exhibit a well-defined peak at values $\omega - \omega_{res} = 0.03$ (mode A, figure 17a) and $\omega - 2\omega_{res} = 0.06$ (mode B, figure 17b; note the difference in the vertical scale between both plots). The mixed-modes solution can thus be viewed in terms of a single helix accompanied by a slaved, phase-locked mode B representing a harmonic deformation due to the resonance. The amplitude of the harmonics is large in the sense of the asymptotic expansion, since both components come at same order. In practice, the amplitude of mode A is however larger, as seen from figures 15(b) and 17(b). It can thus be legitimately expected that the flow solution will resemble a simple helix moderately deformed by its slaved harmonics. Confirmation comes from the reconstruction of the analytical second-order solution, as the modulation induced by the harmonics is not visible from the flow visualization shown in figure 18.

6.2. *Mode selection*

The previous calculations have been repeated at different values of the swirl in order to build a map of the solutions observed in the (S, Re)-plane. The results are synthesized in figure 19 with the colour code already used in figure 11 (the mixed-mode solution being here denoted by the label MM). The critical Reynolds numbers $Re_{NSA,B}$ computed in the non-resonant case are reported as the superimposed dashed lines, and indicate that the size of the hysteresis region is reduced by the resonance, which turns out to be the only significant effect. We therefore conclude that the leading mechanism responsible for the emergence of the double helix in the DNSs is a classical non-resonant interaction between the bifurcating modes.

7. Discussion

We propose now to explain the main dynamical behaviours predicted by the normal form, and in particular the selection of the double helix at sufficiently large Reynolds numbers, consistently with existing numerical results. Unless specified otherwise, all results discussed in the following therefore pertain to the non-resonant double-Hopf interaction analysed in § 5.

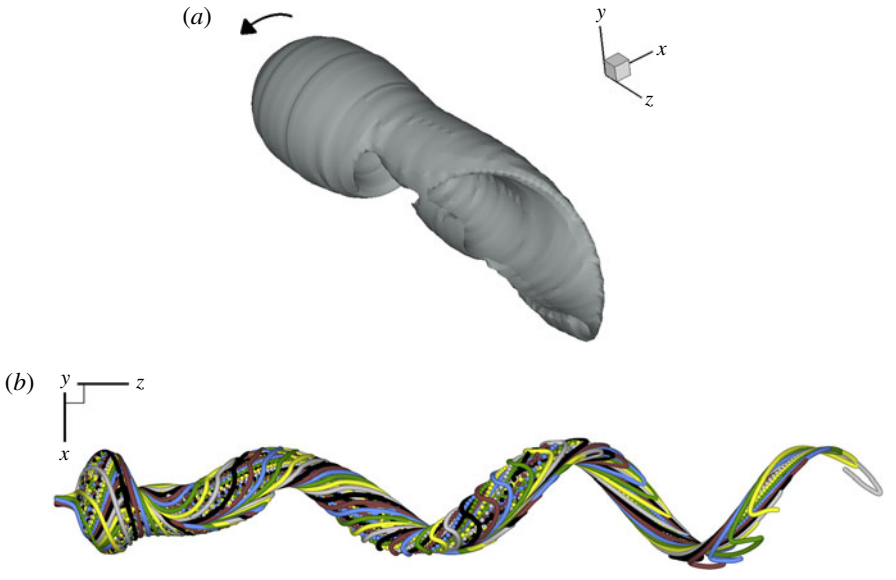

FIGURE 18. (Colour online) Same as figure 12 for the stable mixed-modes solution at $Re = 120$, $S = 1.3$; see supplementary movie 4 for an animation.

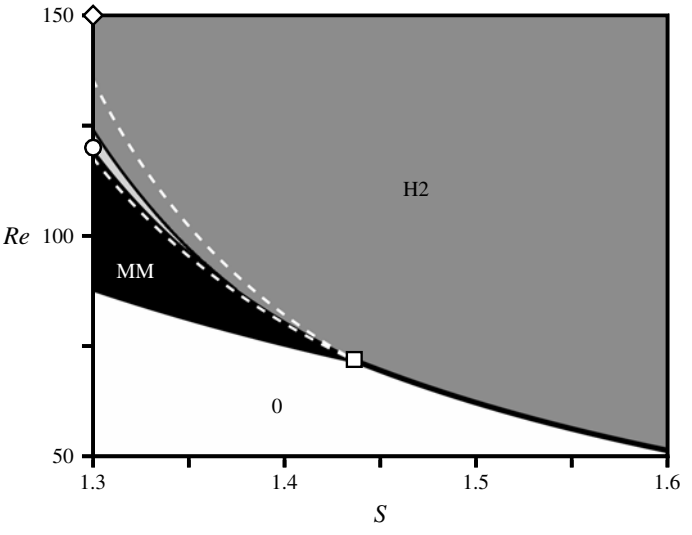

FIGURE 19. Same as figure 11 for the nonlinear patterns predicted by the normal form (6.1). The white dashed lines denotes the upper and lower bounds of the hysteretic domain identified in the non-resonant case, reproduced from figure 11.

7.1. *Damping of mode A*

In the following, we define by σ_{HA} and σ_{HB} the growth rates of small-amplitude, pure disturbances $(A, 0)$ and $(0, B)$ superimposed on the trivial solution. Similarly, σ_{NSA} is the growth rate of pure disturbances $(A, 0)$ superimposed on the double helix, and σ_{NSB} is that of pure disturbances $(0, B)$ superimposed on the simple helix. Simple analytical

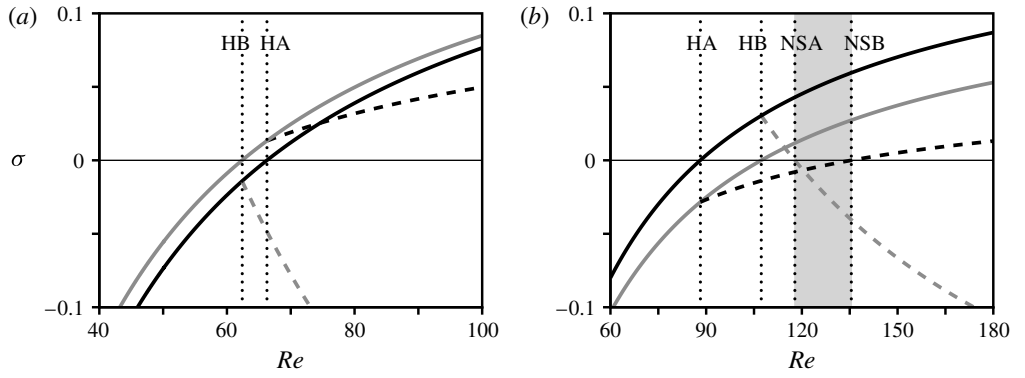

FIGURE 20. Growth rates of modes A and B as a function of the Reynolds number, as computed from relations (7.1). The solid and dashed black lines denote respective values of σ_{HA} and σ_{NSA} while the solid and dashed grey lines denote respective values of σ_{HB} and σ_{NSB}: (*a*) $S = 1.5$; (*b*) $S = 1.3$. The grey shade in (*b*) indicates the domain $[Re_{NSA}; Re_{NSB}]$ where the system is hysteretic.

expressions can be obtained by linearizing the normal form accordingly, which yields

$$\sigma_{HA} = \alpha_{Ar}\left(\frac{1}{Re_c} - \frac{1}{Re}\right) + \beta_{Ar}(S_c - S), \tag{7.1a}$$

$$\sigma_{HB} = \alpha_{Br}\left(\frac{1}{Re_c} - \frac{1}{Re}\right) + \beta_{Br}(S_c - S), \tag{7.1b}$$

$$\sigma_{NSA} = \left(\alpha_{Ar} - \alpha_{Br}\frac{\nu_{Ar}}{\mu_{Br}}\right)\left(\frac{1}{Re_c} - \frac{1}{Re}\right) + \left(\beta_{Ar} - \beta_{Br}\frac{\nu_{Ar}}{\mu_{Br}}\right)(S_c - S), \tag{7.1c}$$

$$\sigma_{NSB} = \left(\alpha_{Br} - \alpha_{Ar}\frac{\nu_{Br}}{\mu_{Ar}}\right)\left(\frac{1}{Re_c} - \frac{1}{Re}\right) + \left(\beta_{Br} - \beta_{Ar}\frac{\nu_{Br}}{\mu_{Ar}}\right)(S_c - S). \tag{7.1d}$$

Figure 20 shows the growth rates computed at the swirl $S = 1.5$ and $S = 1.3$, respectively, for which the bifurcation diagrams are represented in figure 10. For $S = 1.5$ (figure 20*a*), mode B is seen to grow first ($Re_{HB} < Re_{HA}$) and the solution bifurcates to the double helix before mode A grows in turn ($Re > Re_{HA}$). Nevertheless, the double helix is stable ($\sigma_{NSA} < 0$, decreasing), while the single helix is unstable ($\sigma_{NSB} > 0$, increasing) and is thus never to be observed. For $S = 1.3$ (figure 20*b*), mode A now grows first ($Re_{HA} < Re_{HB}$) and the solution bifurcates to the simple helix before mode B may grow in turn. At this stage, the simple helix is stable ($\sigma_{NSB} < 0$, increasing) and the double helix is unstable ($\sigma_{NSA} > 0$, decreasing). After the first Neimark–Sacker bifurcation point, the single and double helices are both stable and remain so up to the second Neimark–Sacker bifurcation point. The simple helix has now become unstable ($\sigma_{NSB} > 0$), and the double helix remains the only stable solution ($\sigma_{NSA} < 0$).

The same conclusions hold for any value of the swirl of both sides of the critical swirl. We can therefore conclude from above that a sufficient condition for the emergence of the double helix is

$$\alpha_{Ar} < \alpha_{Br}\frac{\nu_{Ar}}{\mu_{Br}} \quad \text{and} \quad \alpha_{Br} > \alpha_{Ar}\frac{\nu_{Br}}{\mu_{Ar}}, \tag{7.2}$$

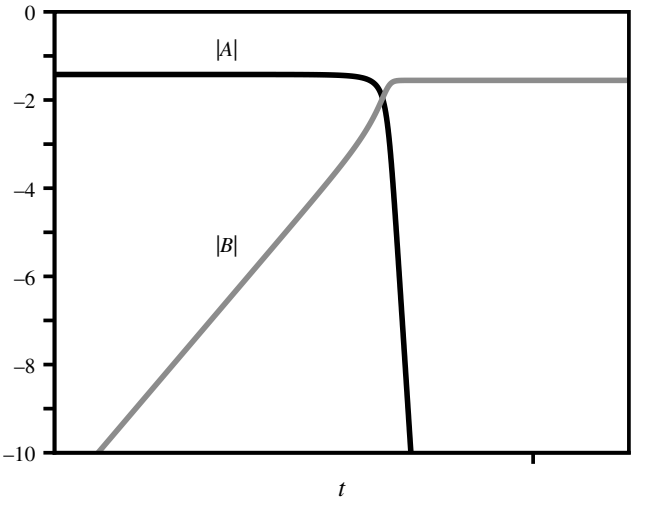

FIGURE 21. Semi-logarithmic plot of the time evolution of the amplitudes obtained from numerical simulations of system (5.1) for $Re = 150$, $S = 1.3$.

or, equivalently,

$$0 < \mu_{Br} < \nu_{Ar} \quad \text{and} \quad \mu_{Ar} > \nu_{Br} > 0, \tag{7.3}$$

since $\alpha_{Ar}/\alpha_{Br} \sim 1$. When increasing the Reynolds number, this guarantees a decrease in σ_{NSA} and an increase in σ_{NSB}, the bifurcation to the double helix occurring at the threshold value Re_{NSB} such that $\sigma_{NSB} = 0$. When this happens, even small amplitudes of mode B are likely to grow, saturate and damp mode A in return, a dynamical behaviour illustrated in figure 21 where we present the time evolution of the amplitudes obtained at $Re = 150$, $S = 1.3$ from a Runge–Kutta simulation of the weakly perturbed trajectories around the limit cycle of the single helix.

7.2. *Interpretation in terms of mean flow corrections and harmonics generation*

It is possible to give insight into the underlying physics by splitting all nonlinear terms into their contributions originating from mean flow corrections and harmonics generation. As has been said already, the Landau coefficient of a given mode (either μ_A or μ_B) stems from two distinct origins, namely the mean flow correction generated by its development and the growth of its first harmonic. In contrast, the coupling coefficient (either ν_A or ν_B) stems from the mean flow correction generated by the development of the other mode and from the growth of two coupled harmonics, i.e. two spiral waves generated by the simultaneous existence of both modes, hence stressing the difference in the physical mechanisms at play. All individual contributions have been computed using the analytical expressions provided in appendix D, where we propose a discussion of these coefficients in novel terms of sensitivity functions to axisymmetric and helical disturbances. We present in table 3 the results pertaining to the real parts, which are those bearing physical relevance in order to unravel the selection mechanism. For the Landau coefficients μ_A and μ_B, the largest contribution comes from mean flow corrections, consistently with the results documented for the single helix at $S = 1$ (§ 4). For the coupling coefficient ν_B, all three contributions are of the same order of magnitude, but both harmonic terms

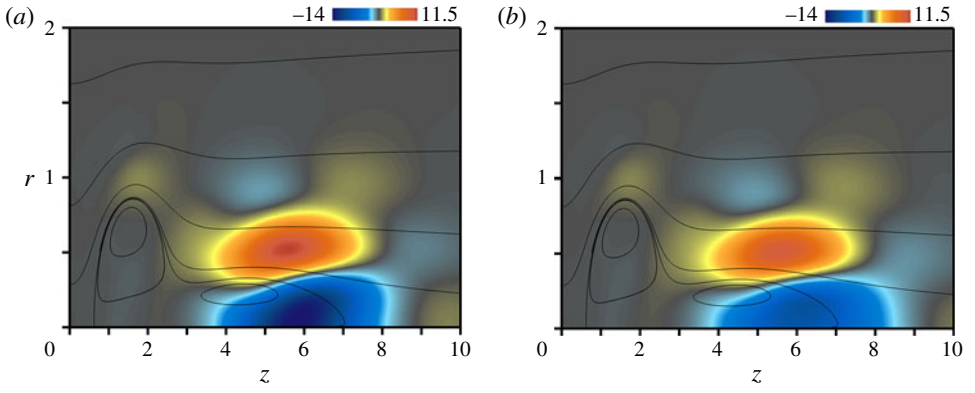

FIGURE 22. (*a*) Spatial distribution of the coupling density field $\nu_{Ar}(r, z)$ yielding the value of the coefficient ν_{Ar} in (5.1). (*b*) Same as (*a*) for the coefficient ν_{Ar} in (6.1). For both plots, $Re = 71.95$, $S = 1.436$.

	Mean flow	Harmonics	Total
μ_A	1.03	0.173	1.20
ν_A	0.674	1.60 + 0.783	3.06
μ_B	0.778	0.0579	0.836
ν_B	0.470	0.352−0.270	0.553

TABLE 3. Decomposition of the nonlinear coefficients of normal form (5.1) into their contribution originating from mean flow correction and harmonics generation. For the coupling coefficients ν_A and ν_B, the values summed in column 3 correspond to the contribution of two distinct harmonics (see appendix D).

almost cancel one another out and we are left in return with a small value satisfying the condition $\mu_{Ar} > \nu_{Br} > 0$ in (7.3). For the coupling coefficient ν_A, both harmonics terms are large and add one with another, which yields the large value satisfying the condition $0 < \mu_{Br} < \nu_{Ar}$ in (7.3). Such results can be synthesized as follows:

(i) the destabilization of the individual modes produces mean flow corrections and harmonics generation;

(ii) the saturation of the pure solutions, i.e. either the single or the double helix, depends on the Landau coefficients and thereby mostly on mean flow corrections;

(iii) the bifurcation from one solution to the other depends on the coupling coefficients and, thereby, mostly on harmonics generation.

We present in figure 22(*a*) the spatial distribution of the coupling density field $\nu_{Ar}(r, z)$, as well as the streamlines of the underlying axisymmetric breakdown solution, made here of two counter-rotating breakdown bubbles. The amplitude is negligible in the primary bubble, but large in the secondary bubble and in its lee, this specific region being the nonlinear coupling region where the competition between harmonics takes place and causes the emergence of the double helix.

	Mean flow	Harmonics	Total
μ_A	1.03	0.269	1.30
ν_A	0.674	$1.24 + 0.787$	2.70
μ_B	0.778	0.0579	0.803
ν_B	0.470	$0.416 - 0.284$	0.602

TABLE 4. Same as table 3 for the nonlinear coefficients of normal form (6.1).

7.3. *Robustness of the proposed mechanism*

Interestingly, the above conclusions carry over from when undertaking the same decomposition in the frame of the resonant normal form analysed in § 6 (we voluntarily forget the coefficients η and χ associated with different second-order resonance mechanisms). From the results reported in table 4, we retrieve that the Landau coefficients μ_A and μ_B are dominated by the contribution of the mean flow corrections, that the coupling coefficient ν_B is small because the harmonic contributions cancel one another out, and that the coupling coefficient ν_A is large because both harmonic contributions add one with another. The same agreement is observed for the localization of the nonlinear coupling regions shown in figure 22(*b*). The consistency of these results, supported by the robustness of the bifurcation structure is somehow remarkable, given the variety of possible dynamical scenarios involved in such complex interactions (over a dozen distinct scenarios for the only double-Hopf interaction).

8. Conclusion

The dynamics of a Grabowski and Berger vortex is investigated using a finite-element discretization method. The existence of spiral breakdown states is shown to proceed from a global instability of the axisymmetric breakdown solution to helical disturbances with azimuthal wavenumbers extending from $m = -1$ to $m = -4$ for the range of swirl and Reynolds numbers considered herein. The transition is led either by the $m = -1$ mode at low and moderate swirl, or by the $m = -2$ mode at large swirl. Both modes develop in the lee of the axisymmetric bubble, not in the immediate vicinity of the stagnation point, and wind in space in the direction opposite to the swirling flow while rotating in time in the same direction, consistently with the DNSs of Ruith *et al.* (2003).

Only the $m = -1$ mode is unstable at low swirl, where the spatio-temporal features of the bifurcated state can be predicted with good accuracy from either a linear or a weakly nonlinear approach. Furthermore, all results agree with existing data issuing either from the DNSs or from the nonlinear front theory of weakly non-parallel flows (Gallaire *et al.* 2006). Both the $m = -1$ and the $m = -2$ modes are simultaneously unstable at moderate swirl, but the 'first to bifurcate' and the 'largest growth rate' criteria neither explain, nor predict, the mode selection observed in the DNSs of Ruith *et al.* (2003). For those regimes, we address the question of mode selection in light of normal form analysis, which allows describing the leading-order nonlinear interactions between modes. The normal form is found to sustain two stable solutions, in addition to the trivial axisymmetric breakdown state. At large swirl, the solution bifurcates to the double helix which keeps being the only stable solution. At low and moderate swirl, it bifurcates first to the single helix, and subsequently to the

double helix through a series of subcritical bifurcations yielding hysteresis over a finite range of Reynolds numbers. The domains of existence of the various solutions predicted in return compare remarkably well with the DNS calculations of Ruith *et al.* (2003). Because the frequencies of the leading modes approach a strong 2:1 resonance, an alternative normal form allowing interactions between the $m = -2$ mode and the harmonics of the $m = -1$ mode is computed and analysed but the effect of the resonance on the bifurcation structure is shown to be limited to a reduction of the hysteresis range. For both cases, we show that the emergence of the double helix is due to competition between harmonics, not to mean flow modifications.

Given the variety of possible dynamical scenarios involved in such complex interactions, the consistency of the results in terms of bifurcation structure, but also in terms of the underlying physics, is somehow remarkable and gives hope that the mechanism selecting the double helix can carry over at moderately large departure from the instability threshold, although confirmation can come only from direct computations of the fully nonlinear 3D Navier–Stokes equations. Those should be in particular developed to probe the existence and extension of a hysteresis region.

Supplementary movies are available at journals.cambridge.org/flm.

Appendix A. Derivation of the normal form for the double-Hopf interaction with 2:1 resonance

This appendix is devoted to the derivation of the analytical resonant normal form (6.1). Unless specified otherwise, all quantities are evaluated at the codimension-two point, i.e. for $Re_c = 71.95$ and $S_c = 1.436$. We carry out a classical asymptotic expansion in terms of a small parameter ϵ representing the order of magnitude of the flow disturbances, for which the analysis consists of expanding the flow field $\boldsymbol{q}$ into

$$\boldsymbol{q} = \boldsymbol{q}_0 + \epsilon \boldsymbol{q}_1 + \epsilon^2 \boldsymbol{q}_2 + \epsilon^3 \boldsymbol{q}_3 + \cdots \tag{A 1}$$

and in computing the flow solutions $\boldsymbol{q}_i$ coming at successive orders in ϵ.

A.1. *Exact* 2:1 *resonance and frequency correction*

As a starting point, we recall that modes A and B are solutions of eigenvalue problems

$$(\mathrm{i}\omega_{cA}\mathscr{N} + \mathscr{L}_{-1c})\,\hat{\boldsymbol{q}}_A = \boldsymbol{0} \quad \text{and} \quad (\mathrm{i}\omega_{cB}\mathscr{N} + \mathscr{L}_{-2c})\,\hat{\boldsymbol{q}}_B = \boldsymbol{0}, \tag{A 2}$$

where $\mathscr{L}_{mc}$ denotes the marginally stable linearized operator. Since we wish to apply the formalism of an exact 2:1 resonant bifurcation, we assume that the detuning between the frequency of mode B and the first harmonic frequency of mode A comes at second order ϵ^2, and introduce the order-unity detuning parameter Δ_ω such that

$$\omega_{cB} - 2\omega_{cA} = 4\epsilon^2 \Delta_\omega. \tag{A 3}$$

This allows the frequencies of the critical eigenmodes to be recast in terms of the resonance frequency ω_{res} defined in (6.2), according to

$$\omega_{cA} = \omega_{res} - \epsilon^2 \Delta_\omega, \quad \omega_{cB} = 2\omega_{res} + 2\epsilon^2 \Delta_\omega. \tag{A 4}$$

In practice, we achieve resonance by expanding the linearized operator into

$$\mathscr{L}_{mc} = \overline{\mathscr{L}}_{mc} + \epsilon^2 \mathscr{S}_m, \tag{A 5}$$

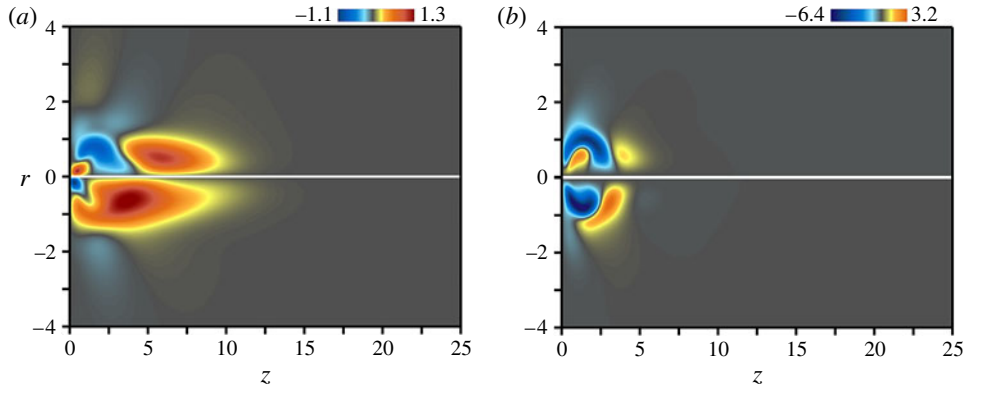

FIGURE 23. (*a*) Spatial distribution of axial velocity for the $m = -1$ adjoint global mode (real part in the upper half of the plot/imaginary part in the lower half). (*b*) Same as (*a*) for the $m = -2$ adjoint global mode – $Re = 71.95$, $S = 1.436$.

for each azimuthal wavenumber m, where $\mathscr{S}_m$ is the so-called shift operator acting according to

$$\mathscr{S}_{-1}\hat{\boldsymbol{q}}_A = \mathrm{i}\Delta_\omega \mathscr{N}\hat{\boldsymbol{q}}_A, \tag{A 6a}$$

$$\mathscr{S}_{-2}\hat{\boldsymbol{q}}_B = -2\mathrm{i}\Delta_\omega \mathscr{N}\hat{\boldsymbol{q}}_B, \tag{A 6b}$$

and

$$\mathscr{S}_m\boldsymbol{q} = \boldsymbol{0} \quad \text{if} \quad \begin{cases} m = 0 \\ m \leqslant -3 \\ m = -1 \quad \text{and} \quad \boldsymbol{q} \neq \hat{\boldsymbol{q}}_A \\ m = -2 \quad \text{and} \quad \boldsymbol{q} \neq \hat{\boldsymbol{q}}_B, \end{cases} \tag{A 7a}$$

$$\mathscr{S}_m\boldsymbol{q} = (\mathscr{S}_{-m}\boldsymbol{q}^*)^* \quad \text{if } m > 0. \tag{A 7b}$$

The key point is that operators $\mathscr{L}_{mc}$ and $\overline{\mathscr{L}}_{mc}$ admit the exact same eigenvectors. These are associated with the exact same eigenvalues, except for the bifurcating global modes that now satisfy the shifted problems

$$(\mathrm{i}\omega_{res}\mathscr{N} + \overline{\mathscr{L}}_{-1c})\,\hat{\boldsymbol{q}}_A = \boldsymbol{0} \quad \text{and} \quad (2\mathrm{i}\omega_{res}\mathscr{N} + \overline{\mathscr{L}}_{-2c})\,\hat{\boldsymbol{q}}_B = \boldsymbol{0}. \tag{A 8}$$

In return, the system exhibits the sought-after 2:1 resonance. Note that expansion (A 5) is only formal, i.e. it is required for the theoretical formalism of resonant bifurcations to apply, but there is no need to construct explicitly either the shifted, or the shift operators.

A.2. *Adjoint global modes and compatibility conditions*

The normal form (6.1) ultimately results from compatibility conditions applied at successive orders in ϵ, whose role is to guarantee the existence of a solution to the expansion (Friedrichs 1973). The enforcement of these conditions relies on the computation of adjoint global modes that can be viewed as Lagrange multipliers for the linearized Navier–Stokes equations (see Meliga *et al.* 2009, for details). We compute here the adjoint modes A and B depicted in figure 23, denoted $\hat{\boldsymbol{q}}_A^\dagger$ and $\hat{\boldsymbol{q}}_B^\dagger$ for

consistency, as the solutions of adjoint eigenvalue problems

$$(-\mathrm{i}\omega_{cA}\,\mathscr{N}+\mathscr{L}^{\dagger}_{-1c})\,\hat{\boldsymbol{q}}^{\dagger}_{A}=\boldsymbol{0}\quad\text{and}\quad(-\mathrm{i}\omega_{cB}\,\mathscr{N}+\mathscr{L}^{\dagger}_{-2c})\,\hat{\boldsymbol{q}}^{\dagger}_{B}=\boldsymbol{0}. \tag{A 9}$$

Operator $\mathscr{L}^{\dagger}_{mc}$ in (A 9) is the adjoint linearized operator, obtained from $\mathscr{L}_{mc}$ by integrating by parts relations (A 2) along with the scalar product

$$\langle\hat{\boldsymbol{a}},\hat{\boldsymbol{b}}\rangle=\int_{\Sigma}\hat{\boldsymbol{a}}\cdot\hat{\boldsymbol{b}}\,r\,\mathrm{d}r\,\mathrm{d}z. \tag{A 10}$$

On account of the frequency shift procedure, the compatibility conditions are however enforced using the equivalent, albeit formal, definitions

$$(-\mathrm{i}\omega_{res}\,\mathscr{N}+\overline{\mathscr{L}}^{\dagger}_{-1c})\,\hat{\boldsymbol{q}}^{\dagger}_{A}=\boldsymbol{0}\quad\text{and}\quad(-2\mathrm{i}\omega_{res}\,\mathscr{N}+\overline{\mathscr{L}}^{\dagger}_{-1c})\,\hat{\boldsymbol{q}}^{\dagger}_{B}=\boldsymbol{0}, \tag{A 11}$$

where operator $\overline{\mathscr{L}}^{\dagger}_{mc}$ is the adjoint operator that would be obtained from the integration by parts of the shifted problems (A 8).

A.3. *Fixed swirl number*

In this section, we prescribe the value of the swirl and set $S=S_c$. We assume that the Reynolds number, which is thus the only varying control parameter, departs from criticality at order ϵ^2 and introduce the order-unity parameter Δ_ν such that

$$\frac{1}{Re}=\frac{1}{Re_c}-\epsilon^2\Delta_\nu. \tag{A 12}$$

We also introduce a fast time scale t and slow time scales $T_i=\epsilon^i t$, so that the time-derivative term in the governing equations is transformed according to

$$\partial_t\to\partial_t+\sum_{i\geqslant 1}\epsilon^i\partial_{T_i}. \tag{A 13}$$

Substitution of the preceding expansions into the governing equations eventually yields a series of equations to be solved at successive orders of ϵ.

At order ϵ^0, the equations are the nonlinear equations (2.6) for $Re=Re_c$ and $S=S_c$, i.e. $\boldsymbol{q}_0$ is the axisymmetric breakdown state computed at the codimension-two point, following the technique described in § 2. At all subsequent orders in ϵ, the solution reads formally

$$\boldsymbol{q}_i=(A_i\hat{\boldsymbol{q}}_A\mathrm{e}^{-\mathrm{i}\theta+\mathrm{i}\omega_{res}t}+B_i\hat{\boldsymbol{q}}_B\mathrm{e}^{-2\mathrm{i}\theta+2\mathrm{i}\omega_{res}t}+\mathrm{c.c.})+\boldsymbol{q}_{i\perp}\quad\forall i\geqslant 1, \tag{A 14}$$

where the complex amplitudes A_i and B_i are at this stage unknown functions of the slow times, and $\boldsymbol{q}_{i\perp}$ is an unknown solution chosen outside the two-dimensional slow manifold, so that the biorthogonality condition (Chomaz 2005) imposes

$$\langle\hat{\boldsymbol{q}}^{\dagger}_{A},\mathscr{N}\boldsymbol{q}_{i\perp}\rangle=\langle\hat{\boldsymbol{q}}^{\dagger}_{B},\mathscr{N}\boldsymbol{q}_{i\perp}\rangle=0. \tag{A 15}$$

A.3.1. *Order one*

The equations at order ϵ^1 are the shifted linearized equations reading

$$(\mathscr{B}\partial_t+\overline{\mathscr{L}}_c)\,\boldsymbol{q}_1=\boldsymbol{0}, \tag{A 16}$$

along with homogeneous boundary conditions. It can be deduced from (A 16) that $\boldsymbol{q}_{1\perp}=\boldsymbol{0}$, meaning that the first-order solution is made up of a superposition of the bifurcating modes

$$\boldsymbol{q}_1=A_1\hat{\boldsymbol{q}}_A\mathrm{e}^{-\mathrm{i}\theta+\mathrm{i}\omega_{res}t}+B_1\hat{\boldsymbol{q}}_B\mathrm{e}^{-2\mathrm{i}\theta+2\mathrm{i}\omega_{res}t}+\mathrm{c.c.}. \tag{A 17}$$

A.3.2. *Order two*

At order ϵ^2, we obtain the linearized Navier–Stokes equations applied to $\boldsymbol{q}_2$

$$(\mathscr{B}\partial_t + \overline{\mathscr{L}}_c)\,\boldsymbol{q}_2 = -\boldsymbol{F}_2, \tag{A 18}$$

along with homogeneous boundary conditions. In (A 18), $\boldsymbol{F}_2$ is the forcing term reading

$$\boldsymbol{F}_2 = \mathscr{N}\,\partial_{T_1}\boldsymbol{q}_1 + \Delta_v \mathscr{D}\boldsymbol{u}_0 + \mathscr{C}[\boldsymbol{u}_1, \boldsymbol{u}_1], \tag{A 19}$$

where we use

$$\mathscr{D}\boldsymbol{a} = \begin{pmatrix} \nabla^2\boldsymbol{a} \\ 0 \end{pmatrix} \quad \text{and} \quad \mathscr{C}[\boldsymbol{a},\boldsymbol{b}] = \begin{pmatrix} \boldsymbol{\nabla a}\cdot\boldsymbol{b} + \boldsymbol{\nabla b}\cdot\boldsymbol{a} \\ 0 \end{pmatrix}, \tag{A 20}$$

for compact notation. The forcing therefore depends on the zeroth- and first-order solutions only. The first term in (A 19) is linear. It corresponds to the slow-time evolution of the first-order solution $\boldsymbol{q}_1$, and generates 4 individual forcing proportional to the amplitudes A_1, A_1^*, B_1 and B_1^*. The second term is also linear. It corresponds to the Reynolds number variation acting here on the base flow, and generates a single forcing proportional to the departure from threshold Δ_v. The third term is nonlinear. It results from the transport of the first-order solution by itself, and generates 10 contributions whose respective amplitudes are obtained by combination of the four first-order amplitudes. The forcing term can thus be split into

$$\boldsymbol{F}_2 = \boldsymbol{F}_{2nr} + \boldsymbol{F}_{2r}, \tag{A 21}$$

with

$$\begin{aligned}\boldsymbol{F}_{2nr} = {} & \Delta_v \mathscr{D}\boldsymbol{u}_0 + |A_1|^2\,\mathscr{C}[\hat{\boldsymbol{u}}_A, \hat{\boldsymbol{u}}_A^*] + |B_1|^2\,\mathscr{C}[\hat{\boldsymbol{u}}_B, \hat{\boldsymbol{u}}_B^*] \\ & + A_1 B_1\,\mathscr{C}[\hat{\boldsymbol{u}}_A, \hat{\boldsymbol{u}}_B]\mathrm{e}^{-3\mathrm{i}\theta+3\mathrm{i}\omega_{res}t} + \text{c.c.} \\ & + \tfrac{1}{2}{B_1}^2\,\mathscr{C}[\hat{\boldsymbol{u}}_B, \hat{\boldsymbol{u}}_B]\mathrm{e}^{-4\mathrm{i}\theta+4\mathrm{i}\omega_{res}t} + \text{c.c.},\end{aligned} \tag{A 22}$$

and

$$\begin{aligned}\boldsymbol{F}_{2r} = {} & (\partial_{T_1} A_1 \mathscr{N}\hat{\boldsymbol{q}}_A + A_1^* B_1\,\mathscr{C}[\hat{\boldsymbol{u}}_A^*, \hat{\boldsymbol{u}}_B])\mathrm{e}^{-\mathrm{i}\theta+\mathrm{i}\omega_{res}t} + \text{c.c.} \\ & + (\partial_{T_1} B_1 \mathscr{N}\hat{\boldsymbol{q}}_B + \tfrac{1}{2}{A_1}^2\,\mathscr{C}[\hat{\boldsymbol{u}}_A, \hat{\boldsymbol{u}}_A])\mathrm{e}^{-2\mathrm{i}\theta+2\mathrm{i}\omega_{res}t} + \text{c.c.}.\end{aligned} \tag{A 23}$$

Each term in (A 22)–(A 23) exhibits a specific azimuthal wavenumber m and frequency ω, and induces in return a response of identical space and time periodicity. The terms in (A 22) do not resonate in the sense that operator $\mathrm{i}\omega\mathscr{N} + \overline{\mathscr{L}}_{mc}$ is non-degenerate, which can be deduced from our linear stability analyses, where we have assessed the stability of all modes of azimuthal wavenumbers $m = 0$ and $|m| \geqslant 3$. In contrast, all terms in (A 23) resonate since $\mathrm{i}\omega_{res}\mathscr{N} + \overline{\mathscr{L}}_{-1c}$ and $2\mathrm{i}\omega_{res}\mathscr{N} + \overline{\mathscr{L}}_{-2c}$ are degenerate operators, whose kernels are precisely spanned by the bifurcating eigenmodes. To avoid secular terms, or in other words, to be able to solve the expansion at second order, compatibility conditions have to be enforced using the Fredholm alternative (Friedrichs 1973). The latter states that the resonant forcing terms must be orthogonal to the kernel of the adjoint operator, which imposes A_1 and B_1 to obey

$$\partial_{T_1} A_1 = -\eta A_1^* B_1, \tag{A 24a}$$

$$\partial_{T_1} B_1 = -\chi {A_1}^2. \tag{A 24b}$$

In (A 24), η and χ are complex coefficients admitting analytical expressions under the generic form of a scalar product between an adjoint global mode and a resonant forcing term of suitable amplitude, namely

$$\eta = \frac{\langle \hat{\boldsymbol{q}}_A^\dagger, \mathscr{C}[\hat{\boldsymbol{u}}_A^*, \hat{\boldsymbol{u}}_B]\rangle}{\langle \hat{\boldsymbol{q}}_A^\dagger, \mathscr{N}\hat{\boldsymbol{q}}_A\rangle} \quad \text{and} \quad \chi = \frac{1}{2}\frac{\langle \hat{\boldsymbol{q}}_B^\dagger, \mathscr{C}[\hat{\boldsymbol{u}}_A, \hat{\boldsymbol{u}}_A]\rangle}{\langle \hat{\boldsymbol{q}}_B^\dagger, \mathscr{N}\hat{\boldsymbol{q}}_B\rangle}. \tag{A 25}$$

System (A 24) constitutes the set of equations governing the leading-order nonlinear interaction between modes. Coupling is seen to occur only on account of the 2:1 resonance. The resulting dynamics is however of little relevance, since the solution is either zero or diverges to infinity in the absence of any restoring term. This is not too surprising, since the nonlinear mechanisms responsible for the saturation of the amplitudes at a finite level, as well as the linear growth induced by the departure from the critical Reynolds number, actually play at order ϵ^3. This means that the expansion must be pursued up to the following order, and thereby that we must solve for the second-order solution expanded into

$$\boldsymbol{q}_2 = (A_2\hat{\boldsymbol{q}}_A + B_2\hat{\boldsymbol{q}}_B + \text{c.c.}) + \boldsymbol{q}_{2\perp}. \tag{A 26}$$

After substitution of relations (A 24) into (A 23), the resonant forcing term is rewritten conveniently as

$$\begin{aligned}\boldsymbol{F}_{2r} = {} & A_1^* B_1(-\eta\mathscr{N}\hat{\boldsymbol{q}}_A^* + \mathscr{C}[\hat{\boldsymbol{u}}_A^*, \hat{\boldsymbol{u}}_B])\mathrm{e}^{-\mathrm{i}\theta+\mathrm{i}\omega_{res}t} + \text{c.c.} \\ & + {A_1}^2(-\chi\mathscr{N}\hat{\boldsymbol{q}}_B^* + \tfrac{1}{2}\mathscr{C}[\hat{\boldsymbol{u}}_A, \hat{\boldsymbol{u}}_A])\mathrm{e}^{-2\mathrm{i}\theta+2\mathrm{i}\omega_{res}t} + \text{c.c.}.\end{aligned} \tag{A 27}$$

Since the compatibility conditions are now trivially satisfied, $\boldsymbol{q}_{2\perp}$ can be sought as the superposition of the responses to each individual forcing term. This yields

$$\begin{aligned}\boldsymbol{q}_{2\perp} = {} & \Delta_\nu\hat{\boldsymbol{q}}_{\Delta_\nu} + |A_1|^2\hat{\boldsymbol{q}}_{AA^*} + |B_1|^2\hat{\boldsymbol{q}}_{BB^*} \\ & + A_1B_1\hat{\boldsymbol{q}}_{AB}\mathrm{e}^{-3\mathrm{i}\theta+3\mathrm{i}\omega_{res}t} + \text{c.c.} \\ & + {B_1}^2\hat{\boldsymbol{q}}_{BB}\mathrm{e}^{-4\mathrm{i}\theta+4\mathrm{i}\omega_{res}t} + \text{c.c.} \\ & + A_1^*B_1\hat{\boldsymbol{q}}_{A^*B}\mathrm{e}^{-\mathrm{i}\theta+\mathrm{i}\omega_{res}t} + \text{c.c.} \\ & + {A_1}^2\hat{\boldsymbol{q}}_{AA}\mathrm{e}^{-2\mathrm{i}\theta+2\mathrm{i}\omega_{res}t} + \text{c.c.},\end{aligned} \tag{A 28}$$

the biorthogonality condition (A 15) now reading

$$\langle \hat{\boldsymbol{q}}_A^\dagger, \mathscr{N}\hat{\boldsymbol{q}}_{A^*B}\rangle = \langle \hat{\boldsymbol{q}}_B^\dagger, \mathscr{N}\hat{\boldsymbol{q}}_{AA}\rangle = 0. \tag{A 29}$$

As an example, the response $\hat{\boldsymbol{q}}_{AA^*}$ representing the mean flow correction induced by the existence of the unstable mode A is a solution to

$$\overline{\mathscr{L}}_{0c}\,\hat{\boldsymbol{q}}_{AA^*} = \mathscr{C}[\hat{\boldsymbol{u}}_A, \hat{\boldsymbol{u}}_A^*]. \tag{A 30}$$

Since the forcing does not resonate, the operator is invertible and $\hat{\boldsymbol{q}}_{AA^*}$ is computed by performing a simple matrix inversion, for which we use the standard LU solver of the UMFPACK library. (See figure 24*a* for the so-obtained spatial distribution of axial velocity.) All non-resonant terms are handled similarly. For resonant terms, we obtain the flow response from a two-step regularization procedure. Consider, for instance, the flow response $\hat{\boldsymbol{q}}_{A^*B}$ satisfying

$$(\mathrm{i}\omega_{res}\mathscr{N} + \overline{\mathscr{L}}_{-1c})\,\hat{\boldsymbol{q}}_{A^*B} = -\eta\mathscr{N}\hat{\boldsymbol{q}}_A^* + \mathscr{C}[\hat{\boldsymbol{u}}_A^*, \hat{\boldsymbol{u}}_B]. \tag{A 31}$$

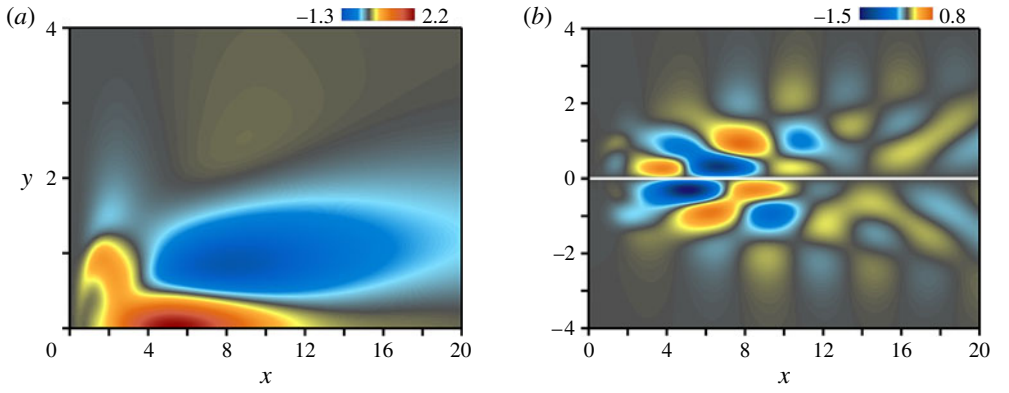

FIGURE 24. (*a*) Spatial distribution of axial velocity for the (real) solution $\hat{\boldsymbol{q}}_{AA^*}$ representing the mean flow correction induced by the existence of the unstable mode A, solution of (A 30). (*b*) Same as (*a*) for the harmonics response $\hat{\boldsymbol{q}}_{A^*B}$, solution of (A 31) (real part in the upper half of the plot/imaginary part in the lower half). For both plots, $Re = 71.95$, $S = 1.436$.

We obtain a particular solution to (A 31) using a specific functionality of the LU solver that treats any zero entry on the diagonal of the upper triangular matrix as if it were equal to one. This is equivalent to solving problem (A 31) using a fictitiously invertible operator acting like the real operator, except on its kernel where it acts like the identity, a technique similar in essence to that discussed by Peyret (2002). If we denote by $\tilde{\boldsymbol{q}}_{A^*B}$ the solution issuing from the modified LU algorithm, the particular solution to (A 31) satisfying the biorthogonality condition (A 29) is thus simply obtained as

$$\hat{\boldsymbol{q}}_{A^*B} = \tilde{\boldsymbol{q}}_{A^*B} - \frac{\langle \hat{\boldsymbol{q}}_A^\dagger, \mathscr{N}\tilde{\boldsymbol{q}}_{A^*B}\rangle}{\langle \hat{\boldsymbol{q}}_A^\dagger, \mathscr{N}\hat{\boldsymbol{q}}_A\rangle}\hat{\boldsymbol{q}}_A, \tag{A 32}$$

the associated spatial distribution of axial velocity being depicted in figure 24(*b*). We follow the same procedure to compute the flow response $\hat{\boldsymbol{q}}_{AA}$ such that

$$(2\mathrm{i}\omega_{res}\mathscr{N} + \overline{\mathscr{L}}_{-2c})\,\hat{\boldsymbol{q}}_{AA} = -\chi\mathscr{N}\hat{\boldsymbol{q}}_B^* + \tfrac{1}{2}\mathscr{C}[\hat{\boldsymbol{u}}_A, \hat{\boldsymbol{u}}_A], \tag{A 33}$$

as

$$\hat{\boldsymbol{q}}_{AA} = \tilde{\boldsymbol{q}}_{AA} - \frac{\langle \hat{\boldsymbol{q}}_B^\dagger, \mathscr{N}\tilde{\boldsymbol{q}}_{AA}\rangle}{\langle \hat{\boldsymbol{q}}_B^\dagger, \mathscr{N}\hat{\boldsymbol{q}}_B\rangle}\hat{\boldsymbol{q}}_B, \tag{A 34}$$

where $\tilde{\boldsymbol{q}}_{AA}$ is the solution issuing from the modified LU algorithm.

A.3.3. *Order three*

At order ϵ^3 we obtain the linearized Navier–Stokes equations applied to $\boldsymbol{q}_3$

$$(\mathscr{B}\partial_t + \overline{\mathscr{L}}_c)\,\boldsymbol{q}_3 = -\boldsymbol{F}_3, \tag{A 35}$$

along with homogeneous boundary conditions. In (A 35), $\boldsymbol{F}_3$ is a new forcing term depending on the zeroth-, first- and second-order solutions, written in compact form as

$$\boldsymbol{F}_3 = \mathscr{S}\boldsymbol{q}_1 + \mathscr{N}\partial_{T_2}\boldsymbol{q}_1 + \mathscr{N}\partial_{T_1}\boldsymbol{q}_2 + \mathscr{D}\boldsymbol{u}_1 + \mathscr{C}[\boldsymbol{u}_1, \boldsymbol{u}_2], \tag{A 36}$$

where $\mathscr{S}$ is the shift operator acting in the real space obtained from $\mathscr{S}_m$ by inverse Fourier transform in the azimuthal direction. The first term in (A 36) is an off-resonance term issuing from the fact that the frequencies of the critical eigenmodes depart from the 2:1 resonance at order ϵ^2. The second and third terms correspond to the slow-time evolution of the lower-order solutions. The fourth term arises from the Reynolds number variation acting here on the first-order solution. Finally, the fifth term is due to the transport of the first-order solution by the second-order solution and vice versa. It splits into two contributions: on the one hand, the linear term $\mathscr{C}[\boldsymbol{u}_1, \boldsymbol{u}_{2\Delta_\nu}]$ taking into account the action of the Reynolds number variation through modifications of the axisymmetric base flow, and on the other hand, numerous nonlinear terms generated by combining the 4 contributions of the first-order solution together with the 10 contributions of the second-order solution.

In order to enforce the required compatibility conditions, and thereby to be able to solve the expansion at third-order, we must identify the resonant terms in (A 36). It can be anticipated that all linear terms resonate, meaning that only the nonlinear terms need to be carefully sorted out. After all calculations have been done, we obtain

$$\boldsymbol{F}_{3r} = \begin{pmatrix} (\partial_{T_1} A_2 + \partial_{T_2} A_1)\mathscr{N}\hat{\boldsymbol{q}}_A \\ + A_1[\Delta_\nu(\mathscr{D}\hat{\boldsymbol{u}}_A + \mathscr{C}[\hat{\boldsymbol{u}}_A, \hat{\boldsymbol{u}}_{\Delta_\nu}]) + \mathrm{i}\Delta_\omega \mathscr{N}\hat{\boldsymbol{q}}_A] \\ + A_1 |A_1|^2(\mathscr{C}[\hat{\boldsymbol{u}}_A, \hat{\boldsymbol{u}}_{AA^*}] + \mathscr{C}[\hat{\boldsymbol{u}}_A^*, \hat{\boldsymbol{u}}_{AA}]) \\ + A_1 |B_1|^2(\mathscr{C}[\hat{\boldsymbol{u}}_A, \hat{\boldsymbol{u}}_{BB^*}] + \mathscr{C}[\hat{\boldsymbol{u}}_B^*, \hat{\boldsymbol{u}}_{AB}] + \mathscr{C}[\hat{\boldsymbol{u}}_B, \hat{\boldsymbol{u}}_{A^*B}^*]) \\ + (A_1^* B_2 + A_2^* B_1)\mathscr{C}[\hat{\boldsymbol{u}}_A^*, \hat{\boldsymbol{u}}_B] \\ - (\eta^* A_1 |B_1|^2 + \chi A_1 |A_1|^2)\mathscr{N}\hat{\boldsymbol{q}}_{A^*B} \end{pmatrix} \mathrm{e}^{-\mathrm{i}\theta + \mathrm{i}\omega_{res} t} + \mathrm{c.c.}$$
$$+ \begin{pmatrix} (\partial_{T_1} B_2 + \partial_{T_2} B_1)\mathscr{N}\hat{\boldsymbol{q}}_B \\ + B_1\left[\Delta_\nu(\mathscr{D}\hat{\boldsymbol{q}}_B + \mathscr{C}[\hat{\boldsymbol{u}}_B, \hat{\boldsymbol{u}}_{\Delta_\nu}]) - 2\mathrm{i}\Delta_\omega \mathscr{N}\hat{\boldsymbol{q}}_B\right] \\ + B_1 |B_1|^2(\mathscr{C}[\hat{\boldsymbol{u}}_B, \hat{\boldsymbol{u}}_{BB^*}] + \mathscr{C}[\hat{\boldsymbol{u}}_B^*, \hat{\boldsymbol{u}}_{BB}]) \\ + B_1 |A_1|^2(\mathscr{C}[\hat{\boldsymbol{u}}_B, \hat{\boldsymbol{u}}_{AA^*}] + \mathscr{C}[\hat{\boldsymbol{u}}_A^*, \hat{\boldsymbol{u}}_{AB}] + \mathscr{C}[\hat{\boldsymbol{u}}_A, \hat{\boldsymbol{u}}_{A^*B}]) \\ + A_1 A_2 \mathscr{C}[\hat{\boldsymbol{u}}_A, \hat{\boldsymbol{u}}_A] \\ - 2\eta B_1 |A_1|^2 \mathscr{N}\hat{\boldsymbol{q}}_{AA} \end{pmatrix} \mathrm{e}^{-2\mathrm{i}\theta + 2\mathrm{i}\omega_{res} t} + \mathrm{c.c.} \tag{A 37}$$

Applying the Fredholm alternative along with the biorthogonality condition (A 29) finally yields

$$\partial_{T_1} A_2 + \partial_{T_2} A_1 = (\alpha_A \Delta_\nu - \mathrm{i}\Delta_\omega) A_1 - \mu_A A_1 |A_1|^2 - \nu_A A_1 |B_1|^2 - \eta\left(A_1^* B_2 + A_2^* B_1\right), \tag{A 38a}$$

$$\partial_{T_1} A_2 + \partial_{T_2} B_1 = (\alpha_B \Delta_\nu + 2\mathrm{i}\Delta_\omega) B_1 - \mu_B B_1 |B_1|^2 - \nu_B B_1 |A_1|^2 - 2\chi A_1 A_2, \tag{A 38b}$$

where η and χ are the complex coefficients already defined in (A 25). All other coefficients admit a similar analytical expression under the form of a scalar product between an adjoint global mode and a resonant forcing term of suitable amplitude.

Namely, the coefficients in (A 38*a*) read

$$\alpha_A = -\frac{\langle \hat{\boldsymbol{q}}_A^\dagger, \mathscr{D}\hat{\boldsymbol{u}}_A + \mathscr{C}[\hat{\boldsymbol{u}}_A, \hat{\boldsymbol{u}}_{\Delta_v}]\rangle}{\langle \hat{\boldsymbol{q}}_A^\dagger, \mathscr{N}\hat{\boldsymbol{q}}_A\rangle}, \tag{A 39a}$$

$$\mu_A = \frac{\langle \hat{\boldsymbol{q}}_A^\dagger, \mathscr{C}[\hat{\boldsymbol{u}}_A, \hat{\boldsymbol{u}}_{AA^*}] + \mathscr{C}[\hat{\boldsymbol{u}}_A^*, \hat{\boldsymbol{u}}_{AA}]\rangle}{\langle \hat{\boldsymbol{q}}_A^\dagger, \mathscr{N}\hat{\boldsymbol{q}}_A\rangle}, \tag{A 39b}$$

$$\nu_A = \frac{\langle \hat{\boldsymbol{q}}_A^\dagger, \mathscr{C}[\hat{\boldsymbol{u}}_A, \hat{\boldsymbol{u}}_{BB^*}] + \mathscr{C}[\hat{\boldsymbol{u}}_B^*, \hat{\boldsymbol{u}}_{AB}] + \mathscr{C}[\hat{\boldsymbol{u}}_B, \hat{\boldsymbol{u}}_{A^*B}^*]\rangle}{\langle \hat{\boldsymbol{q}}_A^\dagger, \mathscr{N}\hat{\boldsymbol{q}}_A\rangle}, \tag{A 39c}$$

and those in (A 38*b*) deduce by permutation of the subscripts A and B.

As the final step in the derivation of the normal form, we unify (A 24)–(A 38) into a single system recast in terms of the physical time t and the total amplitudes

$$A = \epsilon A_1 + \epsilon^2 A_2 \quad \text{and} \quad B = \epsilon B_1 + \epsilon^2 B_2. \tag{A 40}$$

This is achieved by summing (A 24) and (A 38) along with respective weighs ϵ^2 and ϵ^3. We obtain ultimately

$$\mathrm{d}_t A = \left[\alpha_A \left(\frac{1}{Re_c} - \frac{1}{Re}\right) + \mathrm{i}\,(\omega_{cA} - \omega_{res})\right] A - \mu_A A\,|A|^2 - \nu_A A\,|B|^2 - \eta A^* B, \tag{A 41a}$$

$$\mathrm{d}_t B = \left[\alpha_B \left(\frac{1}{Re_c} - \frac{1}{Re}\right) + \mathrm{i}\,(\omega_{cB} - 2\omega_{res})\right] B - \mu_B B\,|B|^2 - \nu_B B\,|A|^2 - \chi A^2, \tag{A 41b}$$

i.e. the analytical normal form is identical to its counterpart (6.1) predicted from symmetry considerations, provided we define the λ coefficients as

$$\lambda_A = \alpha_A \left(\frac{1}{Re_c} - \frac{1}{Re}\right) + \mathrm{i}\,(\omega_{cA} - \omega_{res})\,, \tag{A 42a}$$

$$\lambda_B = \alpha_B \left(\frac{1}{Re_c} - \frac{1}{Re}\right) + \mathrm{i}\,(\omega_{cB} - 2\omega_{res})\,. \tag{A 42b}$$

A.4. *Variable swirl number*

We now let the swirl vary in the vicinity of the critical value S_c. Departure from threshold is assumed to be of order ϵ^2, and we introduce the order unity parameter Δ_s such that

$$S = S_c - \epsilon^2 \Delta_s. \tag{A 43}$$

Substitution of (A 43) into the governing equations yields an additional series of boundary conditions to be satisfied at the inlet:

$$\boldsymbol{u}_0(r, 0) = (0, S_c \Psi(r), 1)^{\mathrm{T}}, \tag{A 44a}$$

$$\boldsymbol{u}_1(r, 0) = \boldsymbol{0}, \tag{A 44b}$$

$$\boldsymbol{u}_2(r, 0) = -\,(0, \Delta_s \Psi(r), 0)^{\mathrm{T}}, \tag{A 44c}$$

$$\boldsymbol{u}_3(r, 0) = \boldsymbol{0}\,\cdots. \tag{A 44d}$$

One sees that the expansion is affected only at order ϵ^2, where condition (A 44*c*) directly adds on to the non-resonant forcing terms, since the velocity profile imposed at the inlet is steady and axisymmetric. This means that enforcing the second-order

compatibility conditions yields the same system of (A 24). In contrast, the orthogonal second-order flow solution $\boldsymbol{q}_{2\perp}$ is modified according to

$$\boldsymbol{q}_{2\perp} \longrightarrow \boldsymbol{q}_{2\perp} + \Delta_s \hat{\boldsymbol{q}}_{\Delta_s}, \tag{A 45}$$

where $\hat{\boldsymbol{q}}_{\Delta_s}$ is the additional response induced by the variation of the swirl, obtained by solving

$$\overline{\mathscr{L}}_{0c}\, \hat{\boldsymbol{q}}_{\Delta_s} = \boldsymbol{0}, \tag{A 46}$$

along with the inlet condition

$$\hat{\boldsymbol{u}}_{\Delta_s}(r, 0) = -\,(0, \Psi(r), 0)^{\mathrm{T}}. \tag{A 47}$$

At order ϵ^3, this additional response interacts nonlinearly with the first-order solution, so that the resonant forcing term (A 37) must be modified according to

$$\boldsymbol{F}_{3r} \longrightarrow \boldsymbol{F}_{3r} + (A_1\, \mathscr{C}[\hat{\boldsymbol{u}}_A, \hat{\boldsymbol{u}}_{\Delta_s}]\mathrm{e}^{-\mathrm{i}\theta+\mathrm{i}\omega_{res}t} + B_1\, \mathscr{C}[\hat{\boldsymbol{u}}_B, \hat{\boldsymbol{u}}_{\Delta_s}]\mathrm{e}^{-2\mathrm{i}\theta+2\mathrm{i}\omega_{res}t} + \mathrm{c.c.}). \tag{A 48}$$

Applying the compatibility condition, we obtain now

$$\begin{aligned}\partial_{T_1} A_2 + \partial_{T_2} A_1 = {} & (\alpha_A \Delta_\nu + \beta_A \Delta_s - \mathrm{i}\Delta_\omega)\, A_1 \\ & - \mu_A A_1 |A_1|^2 - \nu_A A_1 |B_1|^2 - \eta \left(A_1^* B_2 + A_2^* B_1\right), \qquad (\mathrm{A}\,49a)\\ \partial_{T_1} A_2 + \partial_{T_2} B_1 = {} & (\alpha_B \Delta_\nu + \beta_B \Delta_s + 2\mathrm{i}\Delta_\omega)\, B_1 \\ & - \mu_B B_1 |B_1|^2 - \nu_B B_1 |A_1|^2 - 2\chi A_1 A_2, \qquad (\mathrm{A}\,49b)\end{aligned}$$

where the new coefficients β_A and β_B are defined as

$$\beta_A = -\frac{\langle \hat{\boldsymbol{q}}_A^\dagger, \mathscr{C}[\hat{\boldsymbol{u}}_A, \hat{\boldsymbol{u}}_{\Delta_s}]\rangle}{\langle \hat{\boldsymbol{q}}_A^\dagger, \mathscr{N}\hat{\boldsymbol{q}}_A\rangle} \quad \text{and} \quad \beta_B = -\frac{\langle \hat{\boldsymbol{q}}_A^\dagger, \mathscr{C}[\hat{\boldsymbol{u}}_B, \hat{\boldsymbol{u}}_{\Delta_s}]\rangle}{\langle \hat{\boldsymbol{q}}_B^\dagger, \mathscr{N}\hat{\boldsymbol{q}}_B\rangle}. \tag{A 50}$$

The analytical normal form resulting from the unification of the second- and third-order amplitude equations finally remains identical to its counterpart (6.1) predicted from symmetry considerations, provided we now define the λ coefficients as

$$\lambda_A = \alpha_A \left(\frac{1}{Re_c} - \frac{1}{Re}\right) + \beta_A (S_c - S) + \mathrm{i}\,(\omega_{cA} - \omega_{res}), \tag{A 51a}$$

$$\lambda_B = \alpha_B \left(\frac{1}{Re_c} - \frac{1}{Re}\right) + \beta_B (S_c - S) + \mathrm{i}\,(\omega_{cB} - 2\omega_{res}). \tag{A 51b}$$

Provided that the complex amplitudes A and B are obtained from the resolution of the normal form, the nonlinear second-order solution can be analytically reconstructed as

$$\boldsymbol{q} = \boldsymbol{q}_0 + \epsilon \boldsymbol{q}_1 + \epsilon^2 \boldsymbol{q}_2, \tag{A 52}$$

with $\boldsymbol{q}_1$ and $\boldsymbol{q}_2$ the individual solutions defined respectively in (A 17) and in (A 26)–(A 28), which yields

$$\begin{aligned}\boldsymbol{q} = {} & \boldsymbol{q}_0 + \Delta_\nu \hat{\boldsymbol{q}}_{\Delta_\nu} + \Delta_s \hat{q}_{\Delta_s} + |A|^2\, \hat{\boldsymbol{q}}_{AA^*} + |B|^2\, \hat{\boldsymbol{q}}_{BB^*} \\ & + (A\hat{\boldsymbol{q}}_A + A^* B \hat{\boldsymbol{q}}_{A^*B})\mathrm{e}^{-\mathrm{i}\theta+\mathrm{i}\omega_{res}t} + \mathrm{c.c.} \\ & + (B\hat{\boldsymbol{q}}_B + A^2 \hat{\boldsymbol{q}}_{AA})\mathrm{e}^{-2\mathrm{i}\theta+2\mathrm{i}\omega_{res}t} + \mathrm{c.c.} \\ & + AB\hat{\boldsymbol{q}}_{AB}\mathrm{e}^{-3\mathrm{i}\theta+3\mathrm{i}\omega_{res}t} + \mathrm{c.c.} \\ & + B^2 \hat{\boldsymbol{q}}_{BB}\mathrm{e}^{-4\mathrm{i}\theta+4\mathrm{i}\omega_{res}t} + \mathrm{c.c.}, \end{aligned} \tag{A 53}$$

after truncation at order ϵ^2. This expression is that used to generate the isosurfaces of vorticity and the numerical dye lines used to visualize the nonlinear bifurcated flows.

Appendix B. Derivation of the normal form for the double-Hopf interaction

We derive now the analytical non-resonant normal form (5.1). As previously, all quantities are evaluated at the codimension-two point, i.e. $Re_c = 71.95$ and $S_c = 1.436$. Since we consider only the classical interaction between non-resonant modes, no frequency correction is applied, which means that the direct and adjoint modes are solutions of the original eigenvalue problems (A 2)–(A 9), and that the marginal frequencies involved in the expansion are the exact frequencies ω_{cA} and ω_{cB}.

We prescribe first the value of the swirl $S = S_c$ and repeat the procedure detailed in appendix A.3. The first-order solution is similarly chosen as a superposition of the bifurcating modes

$$\boldsymbol{q}_1 = A_1\hat{\boldsymbol{q}}_A \mathrm{e}^{-\mathrm{i}\theta+\mathrm{i}\omega_{cA}t} + B_1\hat{\boldsymbol{q}}_B \mathrm{e}^{-2\mathrm{i}\theta+2\mathrm{i}\omega_{cB}t} + \text{c.c.}. \tag{B 1}$$

The first major difference is found at second order where the forcing terms $\boldsymbol{F}_{2r}$ and $\boldsymbol{F}_{2nr}$ in (A 21) must now read

$$\begin{aligned}\boldsymbol{F}_{2nr} = {} & \Delta_\nu \mathscr{D}\boldsymbol{u}_0 + |A_1|^2\,\mathscr{C}[\hat{\boldsymbol{u}}_A, \hat{\boldsymbol{u}}_A^*] + |B_1|^2\,\mathscr{C}[\hat{\boldsymbol{u}}_B, \hat{\boldsymbol{u}}_B^*] \\ & + A_1^* B_1\,\mathscr{C}[\hat{\boldsymbol{u}}_A^*, \hat{\boldsymbol{u}}_B]\mathrm{e}^{-\mathrm{i}\theta+\mathrm{i}(\omega_{cB}-\omega_{cA})t} + \text{c.c.} \\ & + A_1 B_1\,\mathscr{C}[\hat{\boldsymbol{u}}_A, \hat{\boldsymbol{u}}_B]\mathrm{e}^{-3\mathrm{i}\theta+\mathrm{i}(\omega_{cB}+\omega_{cA})t} + \text{c.c.} \\ & + \tfrac{1}{2}A_1{}^2\,\mathscr{C}[\hat{\boldsymbol{u}}_A, \hat{\boldsymbol{u}}_A]\mathrm{e}^{-2\mathrm{i}\theta+2\mathrm{i}\omega_{cA}t} + \text{c.c.} \\ & + \tfrac{1}{2}B_1{}^2\,\mathscr{C}[\hat{\boldsymbol{u}}_B, \hat{\boldsymbol{u}}_B]\mathrm{e}^{-4\mathrm{i}\theta+2\mathrm{i}\omega_{cB}t} + \text{c.c.},\end{aligned} \tag{B 2}$$

and

$$\boldsymbol{F}_{2r} = \left(\partial_{T_1} A_1 \mathscr{N}\hat{\boldsymbol{q}}_A \mathrm{e}^{-\mathrm{i}\theta+\mathrm{i}\omega_{cA}t} + \partial_{T_1} B_1 \mathscr{N}\hat{\boldsymbol{q}}_B \mathrm{e}^{-2\mathrm{i}\theta+\mathrm{i}\omega_{cB}t}\right) + \text{c.c.}. \tag{B 3}$$

In return, the second-order compatibility condition yields trivially

$$\partial_{T_1} A_1 = 0, \tag{B 4a}$$

$$\partial_{T_1} B_1 = 0. \tag{B 4b}$$

When pursuing the expansion to the third order, the resonant forcing term $\boldsymbol{F}_{3r}$ is

$$\begin{aligned}\boldsymbol{F}_{3r} = {} & \begin{pmatrix} (\partial_{T_1} A_2 + \partial_{T_2} A_1)\mathscr{N}\hat{\boldsymbol{q}}_A \\ + A_1\left[\Delta_\nu(\mathscr{D}\hat{\boldsymbol{u}}_A + \mathscr{C}[\hat{\boldsymbol{u}}_A, \hat{\boldsymbol{u}}_{\Delta_\nu}])\right] \\ + A_1\,|A_1|^2(\mathscr{C}[\hat{\boldsymbol{u}}_A, \hat{\boldsymbol{u}}_{AA^*}] + \mathscr{C}[\hat{\boldsymbol{u}}_A^*, \hat{\boldsymbol{u}}_{AA}]) \\ + A_1\,|B_1|^2(\mathscr{C}[\hat{\boldsymbol{u}}_A, \hat{\boldsymbol{u}}_{BB^*}] + \mathscr{C}[\hat{\boldsymbol{u}}_B^*, \hat{\boldsymbol{u}}_{AB}] + \mathscr{C}[\hat{\boldsymbol{u}}_B, \hat{\boldsymbol{u}}_{A^*B}^*]) \\ + (A_1^* B_2 + A_2^* B_1)\mathscr{C}[\hat{\boldsymbol{u}}_A^*, \hat{\boldsymbol{u}}_B] \end{pmatrix} \mathrm{e}^{-\mathrm{i}\theta+\mathrm{i}\omega_{cA}t} + \text{c.c.} \\ & + \begin{pmatrix} (\partial_{T_1} B_2 + \partial_{T_2} B_1)\mathscr{N}\hat{\boldsymbol{q}}_B \\ + B_1\left[\Delta_\nu(\mathscr{D}\hat{\boldsymbol{q}}_B + \mathscr{C}[\hat{\boldsymbol{u}}_B, \hat{\boldsymbol{u}}_{\Delta_\nu}])\right] \\ + B_1\,|B_1|^2(\mathscr{C}[\hat{\boldsymbol{u}}_B, \hat{\boldsymbol{u}}_{BB^*}] + \mathscr{C}[\hat{\boldsymbol{u}}_B^*, \hat{\boldsymbol{u}}_{BB}]) \\ + B_1\,|A_1|^2(\mathscr{C}[\hat{\boldsymbol{u}}_B, \hat{\boldsymbol{u}}_{AA^*}] + \mathscr{C}[\hat{\boldsymbol{u}}_A^*, \hat{\boldsymbol{u}}_{AB}] + \mathscr{C}[\hat{\boldsymbol{u}}_A, \hat{\boldsymbol{u}}_{A^*B}]) \\ + A_1 A_2\,\mathscr{C}[\hat{\boldsymbol{u}}_A, \hat{\boldsymbol{u}}_A] \end{pmatrix} \mathrm{e}^{-2\mathrm{i}\theta+\mathrm{i}\omega_{cB}t} + \text{c.c.},\end{aligned} \tag{B 5}$$

and the compatibility condition therefore yields

$$\partial_{T_1} A_2 + \partial_{T_2} A_1 = \alpha_A \Delta_\nu A_1 - \mu_A A_1 |A_1|^2 - \nu_A A_1 |B_1|^2, \tag{B 6a}$$

$$\partial_{T_1} A_2 + \partial_{T_2} B_1 = \alpha_B \Delta_\nu B_1 - \mu_B B_1 |B_1|^2 - \nu_B B_1 |A_1|^2, \tag{B 6b}$$

the final system obtained from (B 4)–(B 6) being

$$\mathrm{d}_t A = \alpha_A \left(\frac{1}{Re_c} - \frac{1}{Re} \right) A - \mu_A A |A|^2 - \nu_A A |B|^2, \tag{B 7a}$$

$$\mathrm{d}_t B = \alpha_B \left(\frac{1}{Re_c} - \frac{1}{Re} \right) B - \mu_B B |B|^2 - \nu_B B |A|^2 . \tag{B 7b}$$

We now let the swirl vary in the vicinity of the critical value S_c and repeat the procedure detailed in appendix A.4, which yields straightforwardly

$$\mathrm{d}_t A = \left[\alpha_A \left(\frac{1}{Re_c} - \frac{1}{Re} \right) + \beta_A (S_c - S) \right] A - \mu_A A |A|^2 - \nu_A A |B|^2, \tag{B 8a}$$

$$\mathrm{d}_t B = \left[\alpha_B \left(\frac{1}{Re_c} - \frac{1}{Re} \right) + \beta_B (S_c - S) \right] B - \mu_B B |B|^2 - \nu_B B |A|^2 . \tag{B 8b}$$

Finally, the analytically reconstructed nonlinear second-order solution reads

$$\begin{aligned} \boldsymbol{q} = \boldsymbol{q}_0 &+ \Delta_\nu \hat{\boldsymbol{q}}_{\Delta_\nu} + \Delta_s \hat{q}_{\Delta_s} + |A|^2 \hat{\boldsymbol{q}}_{AA^*} + |B|^2 \hat{\boldsymbol{q}}_{BB^*} \\ &+ (A \hat{\boldsymbol{q}}_A \mathrm{e}^{\mathrm{i}\omega_{cA} t} + A^* B \hat{\boldsymbol{q}}_{A^*B} \mathrm{e}^{\mathrm{i}(\omega_{cB} - \omega_{cA})t}) \mathrm{e}^{-\mathrm{i}\theta} + \text{c.c.} \\ &+ (B \hat{\boldsymbol{q}}_B \mathrm{e}^{\mathrm{i}\omega_{cB} t} + A^2 \hat{\boldsymbol{q}}_{AA} \mathrm{e}^{2\mathrm{i}\omega_{cA} t}) \mathrm{e}^{-2\mathrm{i}\theta} + \text{c.c.} \\ &+ AB \hat{\boldsymbol{q}}_{AB} \mathrm{e}^{-3\mathrm{i}\theta + \mathrm{i}(\omega_{cA} + \omega_{cB})t} + \text{c.c.} \\ &+ B^2 \hat{\boldsymbol{q}}_{BB} \mathrm{e}^{-4\mathrm{i}\theta + 2\mathrm{i}\omega_{cB} t} + \text{c.c.}. \end{aligned} \tag{B 9}$$

Note that the expression of all coefficients is identical to that provided in appendix A. In practice, the slight discrepancy in the numerical estimation of the nonlinear coefficients observed by comparing (5.3)–(6.4) is due to the fact that the harmonics second-order solutions $\hat{\boldsymbol{u}}_{AA}$, $\hat{\boldsymbol{u}}_{BB}$, $\hat{\boldsymbol{u}}_{AB}$ and $\hat{\boldsymbol{u}}_{A*B}$ are computed using the marginal frequencies ω_{cA} and ω_{cB} instead of the reasonant frequencies ω_{res} and $2\omega_{res}$.

Appendix C. Derivation of the Stuart–Landau amplitude equation for individual bifurcating modes

We work here in cuts of constant swirl of the (S, Re)-plane and apply the formalism of simple codimension-one bifurcations to the individual modes, the Reynolds number being the only variable parameter. For ease of reading, the main steps are provided only for mode A but the approach carries over straightforwardly to mode B by permuting the subscripts A and B.

The first-order solution is now

$$\boldsymbol{q}_1 = A_1 \hat{\boldsymbol{q}}_A \mathrm{e}^{-\mathrm{i}\theta + \mathrm{i}\omega_{cA} t} + \text{c.c.}, \tag{C 1}$$

the second-order forcing terms $\boldsymbol{F}_{2r}$ and $\boldsymbol{F}_{2nr}$ must read

$$\boldsymbol{F}_{2nr} = \Delta_\nu \mathscr{D} \boldsymbol{u}_0 + |A_1|^2 \mathscr{C}[\hat{\boldsymbol{u}}_A, \hat{\boldsymbol{u}}_A^*] + \left(\tfrac{1}{2} {A_1}^2 \mathscr{C}[\hat{\boldsymbol{u}}_A, \hat{\boldsymbol{u}}_A] \mathrm{e}^{-2\mathrm{i}\theta + 2\mathrm{i}\omega_{cA} t} + \text{c.c.} \right), \tag{C 2}$$

and

$$\boldsymbol{F}_{2r} = \partial_{T_1} A_1 \mathscr{N}\hat{\boldsymbol{q}}_A \mathrm{e}^{-\mathrm{i}\theta+\mathrm{i}\omega_{cA}t} + \text{c.c.}. \tag{C 3}$$

In return, the second-order compatibility condition yields trivially

$$\partial_{T_1} A_1 = 0. \tag{C 4}$$

At third order, the resonant forcing term $\boldsymbol{F}_{3r}$ is

$$\boldsymbol{F}_{3r} = \begin{pmatrix} (\partial_{T_1} A_2 + \partial_{T_2} A_1)\mathscr{N}\hat{\boldsymbol{q}}_A \\ + A_1[\Delta_\nu(\mathscr{D}\hat{\boldsymbol{u}}_A + \mathscr{C}[\hat{\boldsymbol{u}}_A, \hat{\boldsymbol{u}}_{\Delta_\nu}])] \\ + A_1 |A_1|^2(\mathscr{C}[\hat{\boldsymbol{u}}_A, \hat{\boldsymbol{u}}_{AA^*}] + \mathscr{C}[\hat{\boldsymbol{u}}_A^*, \hat{\boldsymbol{u}}_{AA}]) \end{pmatrix} \mathrm{e}^{-\mathrm{i}\theta+\mathrm{i}\omega_{cA}t} + \text{c.c.}, \tag{C 5}$$

and the compatibility condition yields

$$\partial_{T_1} A_2 + \partial_{T_2} A_1 = \alpha_A \Delta_\nu A_1 - \mu_A A_1 |A_1|^2 . \tag{C 6}$$

The final system obtained from (C 4)–(C 6) is

$$\mathrm{d}_t A = \alpha_A \left(\frac{1}{Re_c} - \frac{1}{Re} \right) A - \mu_A A |A|^2, \tag{C 7}$$

and the analytically reconstructed nonlinear second-order solution reads

$$\boldsymbol{q} = \boldsymbol{q}_0 + \Delta_\nu \hat{\boldsymbol{q}}_{\Delta_\nu} + |A|^2 \hat{\boldsymbol{q}}_{AA^*} + \left(A\hat{\boldsymbol{q}}_A \mathrm{e}^{-\mathrm{i}\theta+\mathrm{i}\omega_{cA}t} + \text{c.c.} \right). \tag{C 8}$$

Appendix D. Mean flow correction versus harmonics generation

We derive now the analytical expressions allowing interpretation of the normal form coefficients in terms of individual mean flow corrections and harmonics generation, computed above as part of the second-order solution $\boldsymbol{q}_2$. Such interpretations are generic to any normal form analysed in the article body. For ease of reading, we discuss only the physics underlying the value of the coefficients μ_A and ν_A but the approach carries over straightforwardly to coefficients μ_B and ν_B by permuting the subscripts A and B.

D.1. *Landau coefficient* μ_A

We recall here the expression defining the coefficient μ_A established above:

$$\mu_A = \frac{\langle \hat{\boldsymbol{q}}_A^\dagger, \mathscr{C}[\hat{\boldsymbol{u}}_A, \hat{\boldsymbol{u}}_{AA^*}] + \mathscr{C}[\hat{\boldsymbol{u}}_A^*, \hat{\boldsymbol{u}}_{AA}] \rangle}{\langle \hat{\boldsymbol{q}}_A^\dagger, \mathscr{N}\hat{\boldsymbol{q}}_A \rangle}. \tag{D 1}$$

The Landau coefficient can be split into two scalar products according to

$$\mu_A = \frac{\langle \hat{\boldsymbol{q}}_A^\dagger, \mathscr{C}[\hat{\boldsymbol{u}}_A, \hat{\boldsymbol{u}}_{AA^*}] \rangle}{\langle \hat{\boldsymbol{q}}_A^\dagger, \mathscr{N}\hat{\boldsymbol{q}}_A \rangle} + \frac{\langle \hat{\boldsymbol{q}}_A^\dagger, \mathscr{C}[\hat{\boldsymbol{u}}_A^*, \hat{\boldsymbol{u}}_{AA}] \rangle}{\langle \hat{\boldsymbol{q}}_A^\dagger, \mathscr{N}\hat{\boldsymbol{q}}_A \rangle}. \tag{D 2}$$

By performing a standard integration by parts, both contributions are recast into

$$\mu_A = \underbrace{-\frac{\langle \mathscr{H}[\hat{\boldsymbol{u}}_A^*, \hat{\boldsymbol{u}}_A^\dagger], \hat{\boldsymbol{q}}_{AA^*} \rangle}{\langle \hat{\boldsymbol{q}}_A^\dagger, \mathscr{N}\hat{\boldsymbol{q}}_A \rangle}}_{\mu_{A,AA^*}} \underbrace{-\frac{\langle \mathscr{H}[\hat{\boldsymbol{u}}_A, \hat{\boldsymbol{u}}_A^\dagger], \hat{\boldsymbol{q}}_{AA} \rangle}{\langle \hat{\boldsymbol{q}}_A^\dagger, \mathscr{N}\hat{\boldsymbol{q}}_A \rangle}}_{\mu_{A,AA}}, \tag{D 3}$$

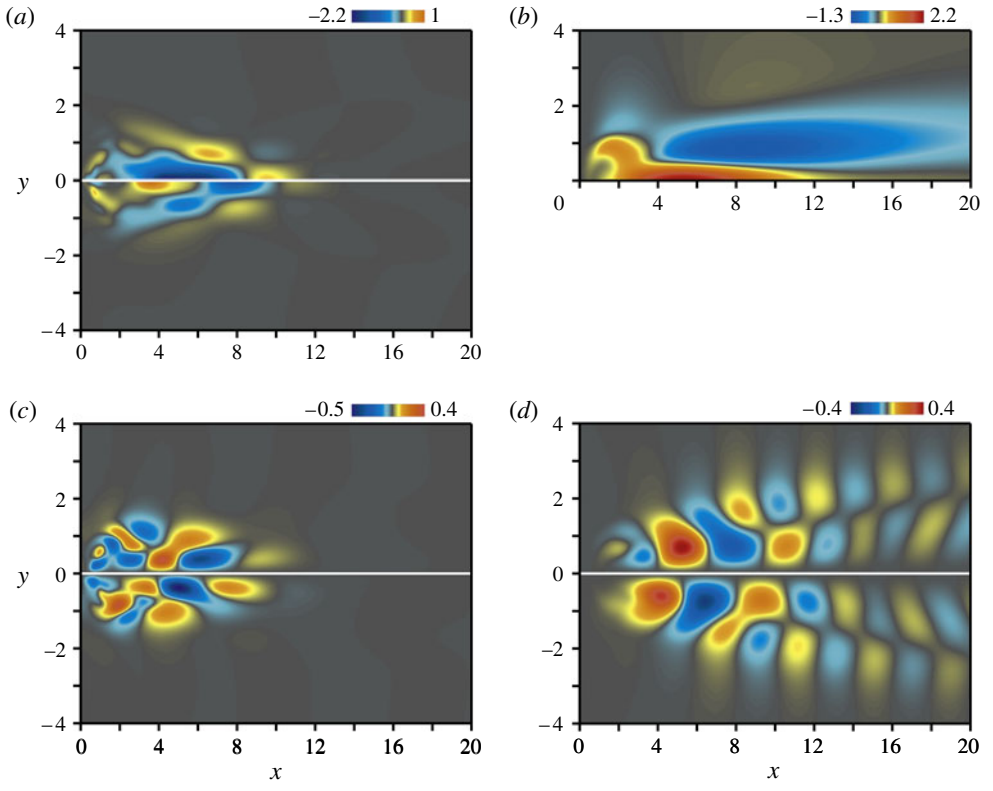

FIGURE 25. (*a*,*b*) Axial components of the (*a*) sensitivity function $\mathscr{H}[\hat{\boldsymbol{u}}_A^*, \hat{\boldsymbol{u}}_A^\dagger]$ to steady, axisymmetric disturbances (real part in the upper half of the plot/imaginary part in the lower half) and (*b*) real mean flow correction $\hat{\boldsymbol{q}}_{AA^*}$. The scalar product between both fields yields the numerical value of the μ_{A,AA^*} coefficient. (*c*,*d*) Axial components of the (*c*) sensitivity function $\mathscr{H}[\hat{\boldsymbol{u}}_A, \hat{\boldsymbol{u}}_A^\dagger]$ to helical disturbances of azimuthal wavenumber $m = -2$ and frequency $\omega = 2\omega_{cA}$ and (*d*) first harmonics $\hat{\boldsymbol{q}}_{AA}$, whose scalar product yields the numerical value of the $\mu_{A,AA}$ coefficient. For all plots, $Re = 71.95$, $S = 1.436$.

where we note

$$\mathscr{H}[\boldsymbol{a}, \boldsymbol{b}] = \begin{pmatrix} -\boldsymbol{\nabla a}^{\mathrm{T}} \cdot \boldsymbol{b} + \boldsymbol{\nabla b} \cdot \boldsymbol{a} \\ 0 \end{pmatrix}. \tag{D 4}$$

Relation (D 3) readily expresses the physical origin of both contributions in the right-hand side. The first term μ_{A,AA^*} is the scalar product of the field $\mathscr{H}[\hat{\boldsymbol{u}}_A^*, \hat{\boldsymbol{u}}_A^\dagger]$ which represents the sensitivity of the flow to steady, axisymmetric disturbances (Bottaro, Corbett & Luchini 2003; Marquet, Sipp & Jacquin 2008), applied here to the mean flow correction $\hat{\boldsymbol{q}}_{AA^*}$ resulting from the existence of mode A. The numerical value of the coefficient therefore depends on a subtle mixing between respective magnitudes, localization and spatial orientation of these two fields, plotted in figure 25(*a*,*b*), respectively. The second term $\mu_{A,AA}$ is the scalar product of the field $\mathscr{H}[\hat{\boldsymbol{u}}_A^*, \hat{\boldsymbol{u}}_A^\dagger]$, viewed as the sensitivity of the flow to helical disturbances of azimuthal wavenumber $m = -2$ and frequency $\omega = 2\omega_{cA}$, applied here to the first harmonics $\hat{\boldsymbol{q}}_{AA}$, both fields being similarly plotted in figure 25(*c*,*d*).

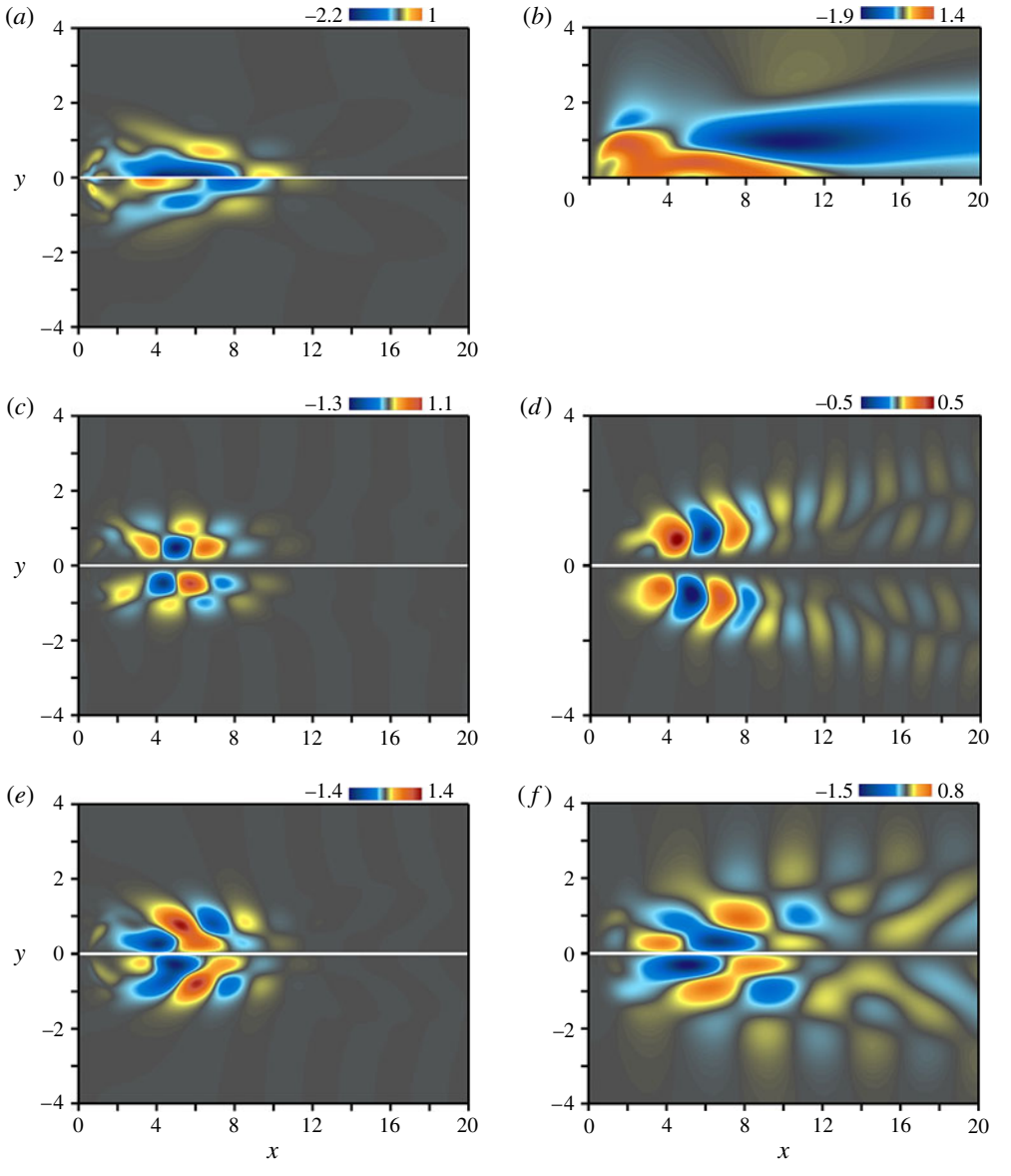

FIGURE 26. (*a*,*b*) Axial components of the (*a*) sensitivity function $\mathscr{H}[\hat{\boldsymbol{u}}_A^*, \hat{\boldsymbol{u}}_A^\dagger]$ already plotted in figure 25(*a*) (real part in the upper half of the plot/imaginary part in the lower half) and (*b*) real mean flow correction $\hat{\boldsymbol{q}}_{BB^*}$. The scalar product of both fields yields the numerical value of the ν_{A,BB^*} coefficient. (*c*,*d*) Axial components of the (*c*) sensitivity function $\mathscr{H}[\hat{\boldsymbol{u}}_B, \hat{\boldsymbol{u}}_A^\dagger]$ and (*d*) harmonics $\hat{\boldsymbol{q}}_{AB}$, whose scalar product yields the numerical value of the $\nu_{A,AB}$ coefficient. (*e*,*f*) Axial components of the (*e*) sensitivity function $\mathscr{H}[\hat{\boldsymbol{u}}_B^*, \hat{\boldsymbol{u}}_A^\dagger]$ and (*f*) harmonics $\hat{\boldsymbol{q}}_{A^*B}$, whose scalar product yields the numerical value of the ν_{A,A^*B} coefficient. For all plots, $Re = 71.95$, $S = 1.436$.

	z_{max}	r_{max}	l	τ	n_t	DoF
M_1	70	10	50	4	279 153	2 776 758
M_2	80	10	50	4	318 237	3 166 230
M_3	70	15	50	4	368 610	3 671 118
M_4	70	10	50	4	452 252	4 505 072
M_5	70	10	60	4	299 690	2 981 324
M_6	70	10	50	2	279 153	2 776 758

TABLE 5. Properties of the meshes as a function of the parameters r_{max}, z_{max}, l and τ. Here n_t is the number of triangles and DoF is the number of degrees of freedom for three-dimensional state vectors. Meshes M_1 to M_3 have the same vertex densities but differ by their spatial extent; M_1 and M_4 have the same spatial extent but M_4 is built with larger vertex densities; M_1 and M_5 differ by the size of the sponge region. Finally, M_1 and M_6 are identical, but calculations on M_6 rely on a different damping function in the sponge region.

	S_0	$\sigma + \mathrm{i}\omega$ $(S = 1/m = -1)$	$\sigma + \mathrm{i}\omega$ $(S = 1.3/m = -1)$	$\sigma + \mathrm{i}\omega$ $(S = 1.3/m = -2)$
M_1	0.890	$0.0387 + 1.16\mathrm{i}$	$0.130 + 1.15\mathrm{i}$	$0.0968 + 2.53\mathrm{i}$
M_2	0.890	$0.0387 + 1.16\mathrm{i}$	$0.129 + 1.15\mathrm{i}$	$0.0964 + 2.53\mathrm{i}$
M_3	0.890	$0.0387 + 1.16\mathrm{i}$	$0.130 + 1.15\mathrm{i}$	$0.0971 + 2.53\mathrm{i}$
M_4	0.890	$0.0385 + 1.16\mathrm{i}$	$0.130 + 1.15\mathrm{i}$	$0.0964 + 2.53\mathrm{i}$
M_5	0.890	$0.0387 + 1.16\mathrm{i}$	$0.130 + 1.15\mathrm{i}$	$0.0968 + 2.53\mathrm{i}$
M_6	0.890	$0.0387 + 1.16\mathrm{i}$	$0.130 + 1.15\mathrm{i}$	$0.0967 + 2.53\mathrm{i}$

TABLE 6. Sensitivity of characteristic numerical values to the different meshes characterized in table 5: the second column provides values of the critical swirl S_0 at which axisymmetric breakdown occurs for $Re = 200$. The second column provides values of the unstable mode A eigenvalue for $Re = 200$, $S = 1$. Finally, the third and fourth columns provides values of the modes A and B eigenvalues for $Re = 200$, $S = 1.3$.

D.2. *Coupling coefficient* ν_A

We focus now on the coupling coefficient ν_A that has been defined as

$$\nu_A = \frac{\langle \hat{\boldsymbol{q}}_A^\dagger, \mathscr{C}[\hat{\boldsymbol{u}}_A, \hat{\boldsymbol{u}}_{BB^*}] + \mathscr{C}[\hat{\boldsymbol{u}}_B^*, \hat{\boldsymbol{u}}_{AB}] + \mathscr{C}[\hat{\boldsymbol{u}}_B, \hat{\boldsymbol{u}}_{A^*B}^*] \rangle}{\langle \hat{\boldsymbol{q}}_A^\dagger, \mathscr{N}\hat{\boldsymbol{q}}_A \rangle}. \tag{D 5}$$

As has been just done for the Landau coefficient μ_A, we can split the scalar product into three distinct terms and integrate by parts, which yields

$$\nu_A = \underbrace{-\frac{\langle \mathscr{H}[\hat{\boldsymbol{u}}_A^*, \hat{\boldsymbol{u}}_A^\dagger], \hat{\boldsymbol{q}}_{BB^*} \rangle}{\langle \hat{\boldsymbol{q}}_A^\dagger, \mathscr{N}\hat{\boldsymbol{q}}_A \rangle}}_{\nu_{A,BB^*}} \underbrace{-\frac{\langle \mathscr{H}[\hat{\boldsymbol{u}}_B, \hat{\boldsymbol{u}}_A^\dagger], \hat{\boldsymbol{q}}_{AB} \rangle}{\langle \hat{\boldsymbol{q}}_A^\dagger, \mathscr{N}\hat{\boldsymbol{q}}_A \rangle}}_{\nu_{A,AB}} \underbrace{-\frac{\langle \mathscr{H}[\hat{\boldsymbol{u}}_B^*, \hat{\boldsymbol{u}}_A^\dagger], \hat{\boldsymbol{q}}_{A^*B} \rangle}{\langle \hat{\boldsymbol{q}}_A^\dagger, \mathscr{N}\hat{\boldsymbol{q}}_A \rangle}}_{\nu_{A,A^*B}}. \tag{D 6}$$

The first term μ_{A,AA^*} in the right-hand side of (D 6) is the scalar product of the sensitivity function to steady, axisymmetric disturbances $\mathscr{H}[\hat{\boldsymbol{u}}_A^*, \hat{\boldsymbol{u}}_A^\dagger]$ already identified in the case of the Landau coefficient, but now applied to the mean flow correction $\hat{\boldsymbol{q}}_{BB^*}$ resulting from the existence of mode B, both fields being represented in figure 26(*a*,*b*). The second term $\mu_{A,AB}$ is the scalar product between the field $\mathscr{H}[\hat{\boldsymbol{u}}_B, \hat{\boldsymbol{u}}_A^\dagger]$, viewed as the sensitivity of the flow to helical disturbances of azimuthal wavenumber $m = -3$ and frequency $\omega = \omega_{cA} + \omega_{cB}$, applied here to the harmonics response $\hat{\boldsymbol{q}}_{AB}$ (figure 26*c*,*d*).

	α_A	β_A	μ_A	ν_A	η
M_1	$15.0+12.3\mathrm{i}$	$-0.282+0.112\mathrm{i}$	$1.30-0.269\mathrm{i}$	$2.70-0.921\mathrm{i}$	$0.112+0.0308\mathrm{i}$
M_2	$15.1+12.3\mathrm{i}$	$-0.281+0.112\mathrm{i}$	$1.30-0.269\mathrm{i}$	$2.70-0.922\mathrm{i}$	$0.111+0.0308\mathrm{i}$
M_3	$15.1+12.3\mathrm{i}$	$-0.281+0.112\mathrm{i}$	$1.30-0.269\mathrm{i}$	$2.71-0.922\mathrm{i}$	$0.112+0.0308\mathrm{i}$
M_4	$15.1+12.3\mathrm{i}$	$-0.281+0.111\mathrm{i}$	$1.30-0.269\mathrm{i}$	$2.69-0.925\mathrm{i}$	$0.112+0.0306\mathrm{i}$
M_5	$15.0+12.3\mathrm{i}$	$-0.281+0.112\mathrm{i}$	$1.30-0.269\mathrm{i}$	$2.70-0.922\mathrm{i}$	$0.112+0.0308\mathrm{i}$
M_6	$15.0+12.3\mathrm{i}$	$-0.282+0.112\mathrm{i}$	$1.30-0.269\mathrm{i}$	$2.70-0.921\mathrm{i}$	$0.112+0.0308\mathrm{i}$
	α_B	β_B	μ_B	ν_B	χ
M_1	$14.1+28.1\mathrm{i}$	$-0.472+0.0961\mathrm{i}$	$0.804-1.08\mathrm{i}$	$0.602-0.0335\mathrm{i}$	$-0.0292+0.164\mathrm{i}$
M_2	$14.1+28.1\mathrm{i}$	$-0.472+0.0961\mathrm{i}$	$0.803-1.08\mathrm{i}$	$0.602-0.0335\mathrm{i}$	$-0.0292+0.164\mathrm{i}$
M_3	$14.0+28.1\mathrm{i}$	$-0.472+0.0961\mathrm{i}$	$0.804-1.08\mathrm{i}$	$0.602-0.0334\mathrm{i}$	$-0.0293+0.164\mathrm{i}$
M_4	$14.1+28.1\mathrm{i}$	$-0.472+0.0956\mathrm{i}$	$0.802-1.08\mathrm{i}$	$0.604-0.0332\mathrm{i}$	$-0.0290+0.164\mathrm{i}$
M_5	$14.1+28.1\mathrm{i}$	$-0.472+0.0958\mathrm{i}$	$0.803-1.08\mathrm{i}$	$0.602-0.0339\mathrm{i}$	$-0.0292+0.164\mathrm{i}$

TABLE 7. Coefficient values of the resonant normal form (6.1) obtained for the different meshes characterized in table 5.

Finally, the third term μ_{A,A^*B} is the scalar product between the field $\mathscr{H}[\hat{\boldsymbol{u}}_B^*, \hat{\boldsymbol{u}}_A^\dagger]$, viewed as the sensitivity of the flow to helical disturbances of azimuthal wavenumber $m = -1$ and frequency $\omega = \omega_{cA} - \omega_{cB}$, applied here to the complex conjugate of the harmonics response $\hat{\boldsymbol{q}}_{A^*B}$ (figure 26*e*,*f*).

Appendix E. Sensitivity of the results to mesh spacing

In order to assess convergence in the numerical results, comparative calculations have been carried out for the meshes M_1 to M_6 detailed in table 5.

In practice, we have computed the swirl at which the vortex breaks down for $Re = 200$, denoted here by S_0. We have also computed the leading eigenvalues for two setting $Re = 200$, $S = 1$ and $Re = 200$, $S = 1.3$, involving both $m = -1$ and $m = -2$ instabilities. Results provided in table 6 indicate that an excellent convergence is achieved, since all values are identical down to the third digit. In particular, it is worth noting that all results are insensitive to the use of sponge regions, hence demonstrating the relevance of the numerical approach. On table 7, the nonlinear coefficients of the resonant normal form (6.1), which turns out to be the most computationally demanding, are compared for the different meshes. Even for those involved calculations, coefficients are converged down to the third digit.

REFERENCES

ABSHAGEN, J., LOPEZ, J. M., MARQUES, F. & PFISTER, G. 2005 Mode competition of rotating waves in reflection-symmetric Taylor–Couette flow. *J. Fluid Mech.* **540**, 269–299.

AVILA, M., MESEGUER, A. & MARQUES, F. 2006 Double hopf bifurcation in corotating spiral Poiseuille flow. *Phys. Fluids* **18** (064101), 1–13.

BILLANT, P., CHOMAZ, J.-M. & HUERRE, P. 1998 Experimental study of vortex breakdown in swirling jets. *J. Fluid Mech.* **376**, 183–219.

BOTTARO, A., CORBETT, P. & LUCHINI, P. 2003 The effect of base flow variation on flow stability. *J. Fluid Mech.* **476**, 293–302.

CHOMAZ, J.-M. 2005 Global instabilities in spatially developing flows: non-normality and nonlinearity. *Annu. Rev. Fluid Mech.* **37**, 357–392.

DAVIS, T. A. 2004 A column pre-ordering strategy for the unsymmetric-pattern multifrontal method. *ACM Trans. Math. Softw.* **30** (2), 165–195 available online from http://www.cise.ufl.edu/research/sparse/umfpack/.

DELBENDE, I., CHOMAZ, J.-M. & HUERRE, P. 1998 Absolute/convective instabilities in the batchelor vortex: a numerical study of the linear impulse response. *J. Fluid Mech.* **355**, 229–254.

DOEDEL, E. J., CHAMPNEYS, A. R., FAIRGRIEVE, T. F., KUZNETSOV, Y. A., SANDSTEDE, B. & WANG, X. 1997 Auto 97: continuation and bifurcation software for ordinary differential equations (with HomCont), Users Guide, available online from http://indy.cs.concordia.ca/auto/.

ESCUDIER, M. 1988 Vortex breakdown: observations and explanations. *Prog. Aerosp. Sci.* **25**, 189–229.

ESCUDIER, M., BORNSTEIN, J. & MAXWORTHY, T. 1982 The dynamics of confined vortices. *Proc. R. Soc. Lond.* A **382**, 335–360.

ESCUDIER, M. & ZEHNDER, N. 1982 Vortex-flow regimes. *J. Fluid Mech.* **115**, 105–121.

FALER, J. & LEIBOVICH, S. 1977 Disrupted states of vortex flow and vortex breakdown. *Phys. Fluids* **20**, 1385–1400.

FRIEDRICHS, K. O. 1973 *Spectral Theory of Operators in Hilbert Space*. Springer.

GALLAIRE, F. & CHOMAZ, J.-M. 2003 Mode selection in swirling jet experiments: a linear stability analysis. *J. Fluid Mech.* **494**, 223–253.

GALLAIRE, F., RUITH, M., MEIBURG, E., CHOMAZ, J.-M. & HUERRE, P. 2006 Spiral vortex breakdown as a global mode. *J. Fluid Mech.* **549**, 71–80.

GRABOWSKI, W. & BERGER, S. 1976 Solutions of the Navier–Stokes equations for vortex breakdown. *J. Fluid Mech.* **75**, 535–544.

GUCKENHEIMER, J. & HOLMES, P. 1983 *Nonlinear Oscillations, Dynamical Systems, and Bifurcations of Vector Fields*. Springer.

HALL, M. 1972 Vortex breakdown. *Annu. Rev. Fluid Mech.* **4**, 195–218.

HECHT, F., PIRONNEAU, O., MORICE, J., LE HYARIC, A. & OHTSUKA, K. 2011 *Freefem++ Manual*, 3rd edn. available online from http://www.freefem.org/ff++/.

HERRADA, M. A. & FERNANDEZ-FERIA, R. 2006 On the development of three-dimensional vortex breakdown in cylindrical regions. *Phys. Fluids* **18** (084105), 1–15.

HUERRE, P. 2000 Open shear flow instabilities. In *Perspectives in Fluid Dynamics* (ed. G. K. Batchelor, H. K. Moffatt & M. G. Worster). pp. 159–229. Cambridge University Press.

KNOBLOCH, E. & PROCTOR, M. R. E. 1988 The double Hopf bifurcation with 2:1 resonance. *Proc. R. Soc. Lond.* A **415**, 61–90.

KUZNETSOV, Y. A. 1998 *Elements of Applied Bifurcation Theory*, 2nd edn. Springer.

LAMBOURNE, N. C. & BRYER, D. W. 1961 The bursting of leading-edge vortices: some observations and discussion of the phenomenon. *Aero. Res. Counc. R&M* **3282**.

LEBLANC, V. G. & LANGFORD, W. F. 1996 Classification and unfoldings of 1:2 resonant hopf bifurcation. *Arch. Rat. Mech. Anal.* **136**, 305–357.

LEHOUCQ, R. B., SORENSEN, D. C. & YANG, C. 1998 *ARPACK Users' Guide: Solution of Large-scale Eigenvalue Problems with Implicitly Restarted Arnoldi Methods*. SIAM, available online from http://www.caam.rice.edu/software/ARPACK/.

LEIBOVICH, S. 1978 The structure of vortex breakdown. *Annu. Rev. Fluid Mech.* **10**, 221–246.

LIM, D. & REDEKOPP, L. 1998 Absolute instability conditions for variable density, swirling jet flows. *Eur. J. Mech. (*B/*Fluids*) **17**, 165–185.

LOISELEUX, T., CHOMAZ, J.-M. & HUERRE, P. 1998 The effect of swirl on jets and wakes: linear instability of the Rankine vortex with axial flow. *Phys. Fluids* **10**, 1120–1134.

LOPEZ, J. M. 2006 Rotating and modulated rotating waves in transitions of an enclosed swirling flow. *J. Fluid Mech.* **553**, 323–346.

MARQUES, F., GELFGAT, A. YU. & LOPEZ, J. M. 2003 Tangent double hopf bifurcation in a differentially rotating cylinder flow. *Phys. Rev.* E **68** (016310), 1–13.

MARQUES, F., LOPEZ, J. M. & SHEN, J. 2002 Mode interactions in an enclosed swirling flow: a double hopf bifurcation between azimuthal wavenumbers 0 and 2. *J. Fluid Mech.* **455**, 263–281.

MARQUET, O., SIPP, D. & JACQUIN, L. 2008 Sensitivity analysis and passive control of the cylinder flow. *J. Fluid Mech.* **615**, 221–252.

MELIGA, P., CHOMAZ, J.-M. & SIPP, D. 2009 Global mode interaction and pattern selection in the wake of a disk: a weakly nonlinear expansion. *J. Fluid Mech.* **633**, 159–189.

MELIGA, P. & GALLAIRE, F. 2011 Control of axisymmetric vortex breakdown in a constricted pipe: nonlinear steady states and weakly nonlinear asymptotic expansions. *Phys. Fluids* **23** (084102), 1–23.

NORE, C., MOISY, F. & QUARTIER, L. 2005 Experimental observation of near-heteroclinic cycles in the von Kármán swirling flow. *Phys. Fluids* **17** (064103), 1–10.

NORE, C., TUCKERMAN, L. S., DAUBE, O. & XIN, S. 2003 The 1:2 mode interaction in exactly counter-rotating von Kármán swirling flow. *J. Fluid Mech.* **477**, 51–88.

PEYRET, R. 2002 *Spectral Methods for Incompressible Viscous Flow*. Springer.

PROVANSAL, M., MATHIS, C. & BOYER, L. 1987 Bénard von Kármán instability: transient and forced regimes. *J. Fluid Mech.* **182**, 1–22.

RUITH, M. R., CHEN, P., MEIBURG, E. & MAXWORTHY, T. 2003 Three-dimensional vortex breakdown in swirling jets and wakes: direct numerical simulation. *J. Fluid Mech.* **486**, 331–378.

SARPKAYA, T. 1971 On stationary and travelling vortex breakdowns. *J. Fluid Mech.* **45**, 545–559.

SPALL, R. E. & GATSKI, T. B. 1991 A computational study of the topology of vortex breadkown. *Proc. R. Soc. Lond.* A **435**, 321–337.

TUCKERMAN, L. S. 2001 Thermosolutal and binary fluid convection as a 2×2 matrix problem. *Physica* D **156**, 325–363.